Padhy *et al.*
Future Journal of Pharmaceutical Sciences (2024) 10:44
https://doi.org/10.1186/s43094-024-00617-1

Future Journal of
Pharmaceutical Sciences

RESEARCH

Open Access

Design, synthesis, 2D-QSAR, molecular dynamic simulation, and biological evaluation of topiramate–phenolic acid conjugates as PPARγ inhibitors

Ipsa Padhy[1], Biswajit Banerjee[1], P. Ganga Raju Achary[2], Pramodkumar P. Gupta[3] and Tripti Sharma[1*]

Abstract

Background Obesity is a precursor for many co-morbid diseases. One of the main triggering factors for obesity is the abnormal expansion of white adipose tissue characterized by high rates of genesis and differentiation of precursor cells into mature adipocytes. As a result, targeting adipogenesis and adipogenic transcription factors opens new roadmaps for developing novel antiobesity pharmacotherapies. The present study was intended to rationally develop topiramate–phenolic acid conjugate for targeting obesity via inhibition of PPARγ which is often considered as the master regulator of adipogenesis.

Results 2D QSAR models were built to foretell PPARγ inhibitory activity of designed conjugates. The models presented excellent robustness, goodness of fit, and predictive capability compounds. The highest PPARγ inhibitory activity was predicted for T3 (topiramate–caffeic acid conjugate) with a pIC_{50} value of 7.08 μM. Molecular docking was performed for all the designed conjugates against PPARγ (PDB ID: 3VSO). The highest binding affinity was exhibited by T3 (−11.27 kcal/mol) and displayed strong and stable interactions with the receptor within the allosteric pocket in comparison to the irreversible PPARγ antagonist, GW9662 (binding affinity, −9.0 kcal/mol). These results were confirmed by subjecting the best-docked molecules to molecular dynamic simulations. The PPARγ–T3 complex was observed to be most stable with maximum number of hydrogen bonds (maximum observed RMSD = 0.57 Å at 100 ns) in comparison to PPARγ–topiramate and PPARγ–caffeic acid complexes. Consequently, T3 was synthesized and further subjected to in vitro screening. The TR-FRET assay established T3 as a PPARγ antagonist (IC_{50} = 6.78 μM). T3 also significantly reduced the lipid buildup in the 3T3-L1 adipocytes in a dose-dependent manner. In addition, T3 also reduced the protein expression levels of PPARγ as evidenced from western blot results.

Conclusions Studies clearly indicated that T3 reduces adipose tissue cell differentiation by downstreaming PPARγ expression at protein levels, thereby emerging as a novel scaffold for antiobesity pharmacotherapy.

Keywords PPARγ, 2D-QSAR, Molecular docking, Molecular dynamic simulation, Antiobesity

*Correspondence:
Tripti Sharma
triptisharma@soa.ac.in
Full list of author information is available at the end of the article

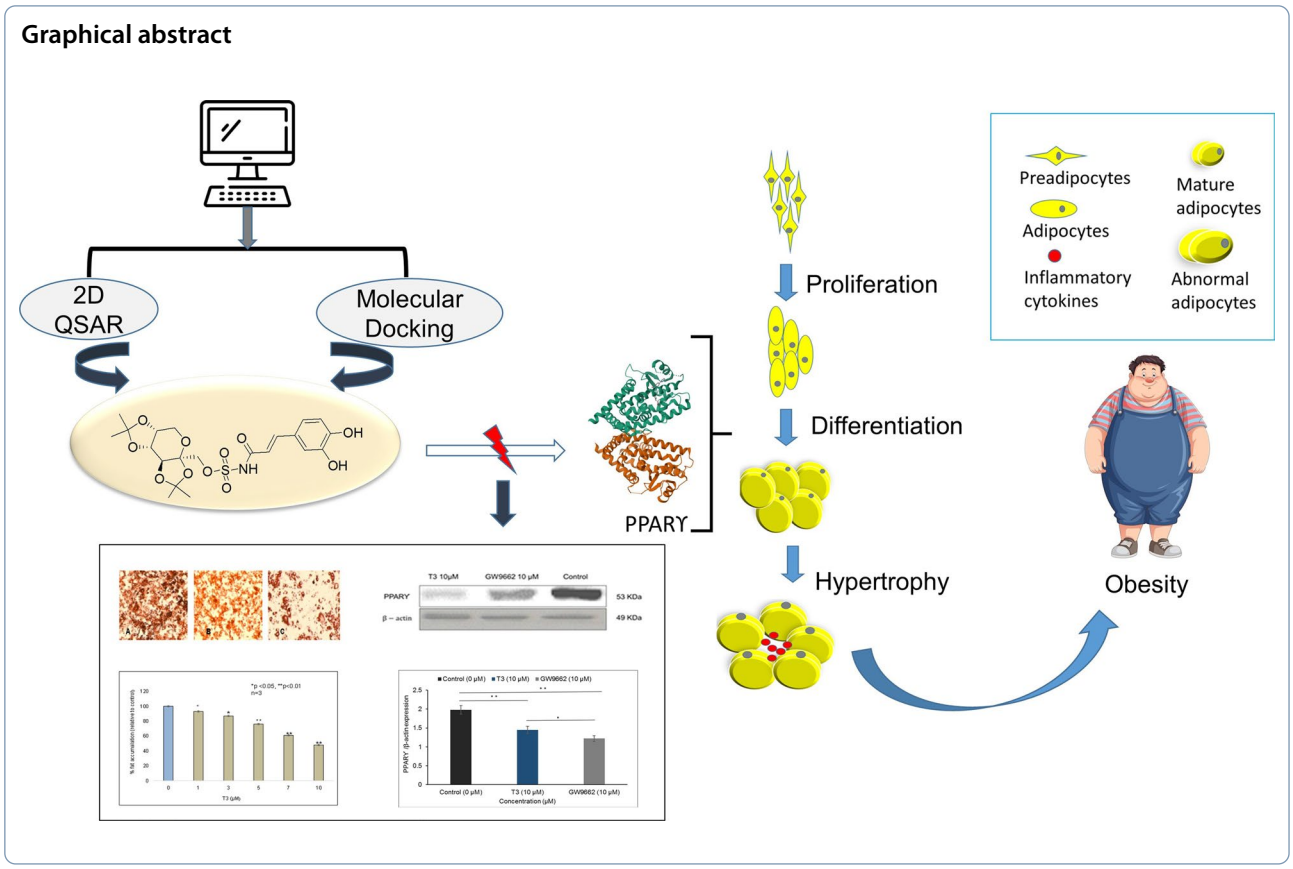

Background

The last decade has laid down a crystal-clear picture of obesity as an ever-increasing global pandemic [1]. Obesity is often associated with co-morbidities encircling type II diabetes, cardiovascular disorders, hypertension, liver dysfunctions, dyslipidemia, obstructive sleep apnea, polycystic ovarian disease, and many cancers. As a master precursor of almost all major chronic metabolic disorders, obesity substantially shoots up the socio-economic burden worldwide by rocketing high healthcare costs [2–7]. Consequently, numerous pharmacotherapeutic agents are developed for the mitigation or cure of obesity by targeting an array of physiological targets, such as pancreatic lipase, 5-hydroxy tryptaminergic receptor 2C, β3 adrenergic receptor, GLP-1 (glucagon-like peptide 1), and many other gut peptides [8] Presently, orlistat, lorcaserin, phentermine/topiramate, bupropion/naltrexone, and liraglutide are approved by FDA (Food and Drug Administration) for obesity pharmacotherapy [9]. Nonetheless, orlistat and lorcaserin have been permitted for longer duration therapy [10, 11]. Incidentally, potential and novel drugs without undesirable physiological adverse actions are the utmost need of the hour for countering obesity.

Topiramate (TPM) is an inhibitor of carbonic anhydrases and glutamate, while acts as an agonist for GABA (γ-aminobutyric acid). It is used for therapy of epilepsy and migraine [12]. Epilepsy patients on TPM medication showed significant weight loss which led to clinical investigation of the drug for having antiobesity effects. In vivo studies have explored thermogenesis boosting and neuro-stabilizing repertoire of TPM [13, 14]. Several studies also discovered that TPM amplified the phosphorylation of crucial lipolytic enzymes, thereby inducing lipolysis in 3T3-L1 preadipocytes. It further suggested TPM might directly inhibit adipogenesis by targeting white adipocytes bypassing its CNS (central nervous system) effect [15].

Phenolic acids are abundantly available from natural sources and are categorized as hydroxy-cinnamic acid derivatives such as caffeic acid (CF), ferulic acid, paracoumaric acid, or hydroxy-benzoic acid derivatives such as gallic acid, chlorogenic acid, protocatechuic acid, or vanillic acid. The phenolic acids basically modulate the gut microbiota in exerting their antiobesity effects [16]. Inhibition of white adipose tissue differentiation, fat browning, pancreatic lipase, and pancreatic amylase inhibition, suppression of inflammatory cytokine

expression, and downregulation of obesity-inducing genes are other pharmacological actions of phenolic acids [17].

The PPARs (peroxisome proliferator-activated receptors) have emerged as promising therapeutic targets among all nuclear receptors for developing novel pharmacotherapeutic candidates against insulin resistance, cancers, obesity, dyslipidemia, and cardiovascular disorders [18]. PPARγ are primarily distributed in adipose tissues and are considered master regulators of adipogenesis [19, 20]. Preferential recruitment of co-repressor molecules over co-activators by PPARγ antagonists as well as close crosstalk with NFκB (nuclear factor kappa B) and AP-1 (activation protein 1) downregulates PPARγ-mediated gene transcription [21, 22]. The medicinal repertoire of PPARγ antagonists spreads more wider than diabetic therapy in promoting osteoblast formation and depressing differentiation of adipose tissue [23]. As a result, PPARγ inhibitors can be well thought out to be potential aspirants for osteoporosis and obesity therapy [24]. Additionally, PPARγ inhibitors embody broad anticancer activity as well [25]. For that reason, exploring PPARγ inhibitors is of prodigious importance in the quest for novel drug candidates for pharmacotherapy of PPARγ-associated metabolic disorders.

Drug-drug conjugates or often called as molecular hybrids comprise of two different pharmacophores interconnected directly or by a spacer (cleavable/non-cleavable). The conjugates usually exert simultaneous action at specific targets with increased potency or efficacy. The high efficacy can be due to improved pharmacokinetic properties. For instance, atorvastatin–curcumin conjugate nanocrystals exhibited enhanced biopharmaceutical and anti-inflammatory properties in comparison to individual drugs [26]. Another striking example is mesalamine–coumarin conjugate with diazo linker displayed an increased anti-inflammatory response by reducing acetic acid-induced ulcerative colitis in rat models [27]. Similarly, nanoparticle of camptothecin–floxuridine conjugate exhibited profound and synergistic anticancer activity with improved cytotoxicity, apoptosis, and inhibition of malignant proliferation [28].

Our present work aims to design and synthesize novel TPAC (topiramate–phenolic acid conjugates). Through robust 2D-QSAR (two-dimensional quantitative structure–activity relationship) models, the biological activity of the designed conjugates was predicted. In silico molecular docking was done for gaining insights of the interaction nature of designed conjugates with the receptor. The MD (molecular dynamic) simulation study revealed good dynamic behavior of PPARγ–T3 complex. Among all the three complexes, PPARγ–T3 had minimum RMSD, RMSF, Rg, and potential energy indicating good attractive and stable interactions between protein and ligand molecules over the total MD simulation time. Lantha Screen TR-FRET assay was performed to evaluate the PPARγ inhibition potency of the designed conjugates. The antiobesity effects of the T3 (topiramate–caffeic acid conjugate) were demonstrated via differentiation inhibition and lipid accumulation in the 3T3-L1 preadipocytes.

Methods

Computational study

QSAR studies

Dataset preparation In the current study, an experimental dataset of 100 compounds was retrieved from the Binding dB database [29]. The biological activities of the compounds were expressed in terms of IC_{50} (nM, half maximal inhibitory concentration) and were converted to their corresponding pIC_{50} values (negative logarithm of IC_{50} values). For building the 2D-QSAR model, pIC_{50} was considered as the dependent variable. The raw dataset compounds and their corresponding IC_{50} values are provided in supplementary files for reference (Additional file 1: Table S1).

Descriptors computation Before the computation of the molecular descriptors, geometry optimization was carried out for each dataset molecule employing molecular mechanics force field and semi-empirical AMI methods using SPARTAN 10.0 software tools. The energy-minimized structures were further used to generate molecular descriptors using two software tools PaDEL and CORAL. PaDEL version 2.21 [30] was used to generate about 1444 2D molecular descriptors. More than 50% of descriptors with zero, missing, and constant values were excluded. Also using pairwise correlation, the descriptors were filtered. The CORAL (http://www.insilico.eu/coral) software generated single optimal descriptor (DCW) [31] basing on SMILES (simplified molecular input line system) [32, 33]. The descriptor is calculated using the Index of ideality of correlation (IIC) formalism which was carried out for the Monte Carlo optimization taking the IIC weight = 0.2000. The details of the calculation of the DCW by IIC are described elsewhere [34, 35]. The PCA (principal component analysis) was applied to determine the best descriptor (variables) combination. The dataset molecules were sorted according to PC1 scores. As a final point, 20 molecular descriptors were utilized for deriving models from the whole data set. The computed molecular descriptors for the 100 dataset compounds are provided in supplementary files for reference (Additional file 1: Table S2).

QSAR modeling The 100 molecules of dataset were split into training set (87 molecules) and validation set (13 mol-

ecules). GA (genetic algorithm) and MLR (multiple linear regression) techniques were employed for building robust QSAR models using QSARINS software [36]. 2D-QSAR models were built using combinations of selected 20 descriptors, including the one optimal descriptor DCW.

QSAR model validation All the developed models were validated according to OECD (Organization for Economic Cooperation and Development) principles using the QSARINS software package. The validation aimed at ensuring that the built models have definite endpoints represented using unambiguous algorithms, have domain of applicability, and have appropriate measures for predictability, goodness of fit, and robustness. Leverage values below critical leverage with ± 3 standard deviations were considered to ensure good predictive capability of designed QSAR models. The compounds remaining outside these leverage values were treated as outliers. Williams's plots were employed to describe QSAR model applicability domain. To minimize the discrepancies between experimental and predicted values of the endpoint, goodness of fit was computed employing R^2 (coefficient of determination) and R^2adj (coefficient of determination adjusted for degrees of freedom). Internal validation methods like LOO (leave one out) and LMO (leave many out) were used to verify and measure the strength of models generated. To ascertain the predictive capability of the designed models, various external validation parameters were analyzed and computed such as RMSE ext, Q^2–F1, Q^2–F2, Q^2–F3, R^2 m, R^2 m delta, CCC, MAE ext and PRESS ext. Finally, Y-scrambling method confirmed that built models are not outcomes of chance correlation.

Prediction of IC_{50} values of novel topiramate–phenolic acid conjugates Ten novel TPAC (T1-T10) were designed using Chemdraw Ultra 12.0 software. Geometry optimization was done for each designed molecule employing molecular mechanics force field and semi-empirical AMI methods using SPARTAN 10.0 software tools (http://www.wavefun.com/products/spartan.html). Further 2D molecular descriptors for the newly designed conjugates were computed using PaDEL software. The single optimal descriptor was also calculated for the designed compounds using CORAL software. The leverage values of all the designed compounds were calculated and compared with the threshold leverage value h^* (0.138). Using the best generated QSAR equation, the pIC_{50} values of the designed molecules were predicted.

Molecular docking

Among the designed conjugates, highest PPARγ inhibitory activity was predicted for the topiramate–caffeic acid conjugate (T3). Accordingly, T3 was selected for molecular docking and molecular dynamic simulation analysis.

Ligand preparation The structure of CF, TPM, and T3 conjugate was drawn in Chemdraw Ultra 12.0 software and stored in standard format (SDF). All the ligands were subjected to energy minimization UCSF Chimera 1.16 [37] prior to docking.

Protein preparation 3-D crystal structure of PPARγ (PDB ID: 3VSO) was retrieved from the RCSB protein bank using Energy minimization and geometry optimization was performed using UCSF Chimera 1.16 by adding hydrogen atoms and charges to the receptor. Finally, the protein was saved in pdbqt format for docking.

Docking AutoDock Vina [38] was used for docking of the ligands with the selected protein. After energy minimizing, a grid box resolution with three dimension coordinates 17.762, 71.66, and 13.333 was set. Grid box with 60 × 60 × 60 Å point spacing of 0.375 Å was used to reformate structure files into pdbqt format. The flexible ligand docking studies were performed using Lamarckian genetic algorithm.

Molecular dynamic simulation

To compare the interaction of individual pharmacophoric ligands CF and TPM with conjugate ligand T3, all the protein–ligand complexes (PPARγ-CF, PPARγ-TPM, and PPARγ-T3) were directed for 100 ns MD (molecular dynamic) simulation using Gromacs 4.5.6 [39]. For generating the topology of a protein–ligand complex system, initially, protein and ligand were separated as a single entity, followed by the generation of individual topology or protein and ligand and finally merging back to complex form. With the help of CHARMM-36 parameters, here we created the topology for proteins (X, Y, Z coordinate system) using TIP 3P water model, and for each ligand we have used Swiss-Param online server to generate the topology. The protein.gro and ligand.gro files were manually fit, and complex.gro was generated for each of the three complexes. Further, the complex file is solvated using SPC216 water model in dodecahedron form with system size as follows: PPARγ-CF complex = X: 5.099, Y: 6.095, and Z: 5.654 (nm). PPARγ-TPM complex = X: 5.099, Y: 6.095, and Z: 5654 (nm). PPARγ-T3 complex = X: 5.099, Y: 6.095 and Z: 5654 (nm). Solvent molecules and sodium ions were added for neutralization of the system.

Further energy of neutralized system was minimized by employing steepest descent minimization method for 50,000 steps. The stability of the complex post energy

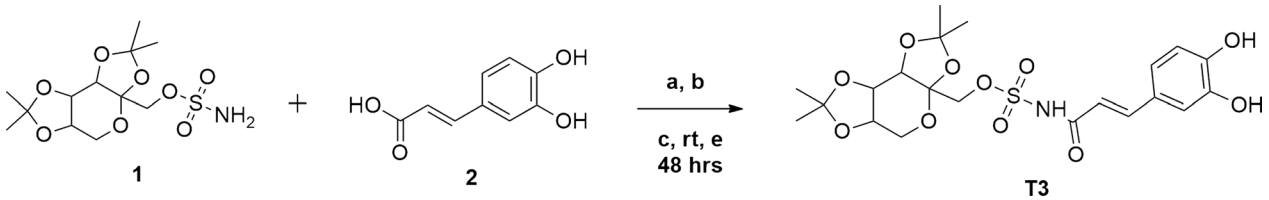

Scheme 1 DCC-DMAP mediated coupling of caffeic acid and topiramate. *Reagents and conditions:* **a** DMAP **b** DCC **c** DMF

minimization is carried out by assessment of potential energy, bond energy, proper dihedral, and improper dihedral. Going beyond the energy minimization, .itp file of restrained ligand position was generated and incorporated into complex topology file using leap-frog integrator algorithm. MD simulation was run for 50,000,000 steps. The system was restrained on covalent bond by employing LINCS algorithm [40]. Following 100 ns MD simulation, the RMSD (root mean square deviation), RMSF (root mean square fluctuation), Rg (radius of gyration), H-bond, and SASA (solvent accessible surface area) were calculated. The graphs were created by XM Grace Linux application, while the two-dimensional interactions were studied in BIOVIA Discovery studio visualizer.

Chemistry

General

3T3-L1 preadipocytes were obtained from NCCS (National Centre for Cell Science), Pune, India. DMEM (Dulbecco's Modified Eagle's Medium), BCS (bovine calf serum), antibiotic solutions, and antibodies for enzyme assay as well as western blot were purchased from Thermo Fisher Scientific, (Waltham, MA, USA). Topiramate was procured from Yucca Chem Products, Mumbai. Other reagents/chemicals (high purity) used were purchased from Sigma-Aldrich (St Louis, USA) and used as received.

Synthesis of topiramate–caffeic acid conjugate, T3

T3 (topiramate–caffeic acid conjugate) was synthesized using DCC-DMAP coupling [41–43]. CF (2), 1 equivalent and DCC (N,N'-dicyclohexyl carbodimide, 1.1 equiv), and DMAP (4-dimethylaminopyridine, catalytic amount, 10 mol%) were added with 20 ml of DMF (dimethylformamide) with continuous stirring for 60 min. After 60 min of stirring, TPM (1), 2 equivalents in excess DMF was added to the above reaction mixture and allowed to stir at room temperature for 48 h (Scheme 1).

The reaction was monitored by TLC (aluminum sheets with Silica-Gel 60 F254 (Merck) employing ethyl acetate/pet ether (7:3) as mobile phase till completion. Following reaction completion, crude reaction mixture was water washed (10 ml) and filtered to remove dicyclohexyl urea (by-product). The filtrate was transferred to a separating funnel and extracted with ethyl acetate (20 ml × 3 times). The organic fraction was further collected and dried over anhydrous Na_2SO_4, and the solvent was removed under reduced pressure. The residue was recrystallized from ethyl acetate. Melting point was determined by open capillary tubes in a melting point apparatus and presented uncorrected. Spectral characterization was further performed (IR using JASCO FTIR-4100 series; ^{1}HNMR and ^{13}CNMR using Bruker 400 MHz NMR spectrophotometer).

Biological screening

In vitro enzyme inhibition assay

PPARγ inhibition was studied using TR-FRET co-activator assay [43]. Concisely, the human recombinant PPARγ-LBD (GST tagged, 1 nmol/L) was incubated with a Europium-labeled anti-GST antibody (2 nmol/L), testing samples, and DMSO (control). Following incubation, SRC (steroid receptor co-activator, XL665 labeled streptavidin) was added. The SRC co-activator peptide (20 nmol/L) was prepared in Tris–HCl (pH 7.4) The fluorescent signals were measured by microplate reader (BMG Labtech, Germany) at an excitation wavelength of 337 nm and emission wavelengths of 620 and 665 nm. The emission ratio was computed using the equation given below:

$$\text{Emission ration (ER)} = \text{fluorescein emission at 665} / \text{fluorescein emission at 620 nm}$$

Agonist mode Fluorescent signals generated from rosiglitazone (positive control, 10 μmol/L) were considered 100% activation control. 1% DMSO was considered as blank/0% activation control. The activation percentage was computed by the below mentioned formula.

$$\%\,\text{Activation (Agonist mode)} = \{\text{ER 1} - \text{ER 2}/\text{ER 3} - \text{ER 2}\} * 100\%$$

where ER 1 is the emission ratio of the sample, ER2 is the emission ratio of the blank, and ER3 is the emission ratio of 100% activation control (10 μmol/L rosiglitazone).

Antagonist mode To the human recombinant PPARγ and co-activator peptide previously incubated with test samples, 1 μM rosiglitazone was incorporated as EC_{80} control. The percentage inhibition of T3 was computed using the below mentioned formula. GW9662, irreversible PPARγ antagonist, was used as positive control.

$$\%\,\text{Inhibition (Antagonist mode)} = \{ER\,1 - ER\,2/ER\,4 - ER\,2\} * 100\%$$

where ER 1 is the emission ratio of sample, ER 2 is the emission ratio of blank, and ER 3 is the emission ratio of EC_{80} (1 μmol/L rosiglitazone).

Inhibition of adipogenesis in 3T3-l1 preadipocytes

Cell culture, differentiation, and maturation The preadipocytes were sub-cultured in DMEM complemented with 10% (v/v) BCS 1% penicillin–streptomycin antibiotic mixture antibiotic in an atmosphere of 5% CO_2 at 37 °C. After 70–80% cell confluency, harvesting was done using 25 mm tissue culture flask containing trypsin and seeding in 96 well plate. After 100% confluency of cells, differentiation was performed by adding insulin (1 μg/mL), isobutyl-1-methylxanthine (0.5 mM/L), and dexamethasone (0.25 μM/L). Post confluency, by careful pipetting the differentiation media was discarded and maturation media (insulin, 1 mg/L) was added and changed every 2 days. The control group remain untreated. The test groups received 1, 5, and 10 μM of T3, respectively. The positive control group was treated with 10 μM of GW9662. Post 10 days, lipid droplets were clearly visible inside the differentiated cells and hence subjected to further assays [44].

MTT assay Cytotoxic effect of T3 on adipocyte precursor cells was investigated through MTT assay [44]. The 3T3-L1 preadipocytes were seeded in 96-well plate (3 × 104 cells per well) and cultured in DMEM containing 10% BCS for 24 h. After 24 h the cells were treated with 0.001, 0.01, 0.1, 1, and 10 μg/mL of T3, respectively, and kept for next 72 h. Post 72 h, MTT (3-(4,5-dimethylthiazol-2-yl)-2,5-diphenyltetrazolium bromide) solution (20 μL, 5 mg mL^{-1}) was added to each well and further incubated for 4 h at 37 °C. The dark blue formazan product formed by the cells was carefully dissolved in DMSO within a dark cabinet, and absorbance was measured at 495 nm in a microplate reader (Bio-Rad Lab, California).

Oil Red O staining To observe lipid droplets within differentiated adipocytes, the Oil O Red stain method was employed. The differentiated cells were initially washed with PBS and then fixed with 4% formaldehyde for 30 min. Further, the cells were stained with freshly prepared (in 60% isopropyl alcohol) Oil O Red solution for 10 min at room temperature. After 10 min the stained cells were rinsed with isopropyl alcohol for extraction of accumulated lipids and their quantification (absorbance measured at 495 nm) in terms of percentage relative to the control. The untreated cells were taken as control. The cells stained were observed under a phase contrast microscope (Axiovert 40 CFL, Carl Zeiss, Jena, Germany) and photographed [44]

Western blot In brief, the cells were rinsed with PBS, lysed using Laemmli buffer (comprising of 62.5 mM Tris–HCl, 10% glycerol, and 2% SDS) and sonicated. 10 μg of protein was separated by gel electrophoresis (10% SDS-PAGE), transferred on to nitrocellulose membrane, and blocked using 5% PBS-T milk (45 min). Anti PPARγ and β-actin antibodies were added to 1% BSA in PBS-T milk and incubated with membrane previously blocked containing protein lysates at room temperature for 1 h. Following incubation, the membrane was washed with PBS-T milk and treated with secondary antibody (HRP-conjugated) following incubation for next 30 min. Then the membranes were washed with PBS-T milk twice for 10 min in room temperature. Chemiluminescence was detected using the ChemiDoc Touch imaging system (Bio-Rad) [45]. β-actin was used as internal control.

Statistical analysis

All the experiments were performed in triplicate. The data from each independent experiment are expressed as mean ± standard deviation. The presented data were statistically analyzed employing one-way ANOVA with *t*-test for defining differences. Values of ($^{*}p < 0.05$ and $^{**}p < 0.01$) were considered statistically significant.

Result

Computational studies

Variable selection by PCA

Data redundancy was reduced employing PCA (principle component analysis). The eigen values were sorted in descending order. PC1 describes greatest data variance, while PC2 described data variance in an orthogonal direction to PC1. Principal component analysis (PCA) for the descriptors VE3_Dzp, nHBint6, and DCW was demonstrated by loading and scoring plots. Figure 1A displays the scoring plot for dataset compounds. Likewise, Fig. 1B displays the loading plot for M-1 descriptors. PCA score plot describes the type of co-relation between dataset components. The loading plot on the other hand describes the influential power of descriptors on dataset

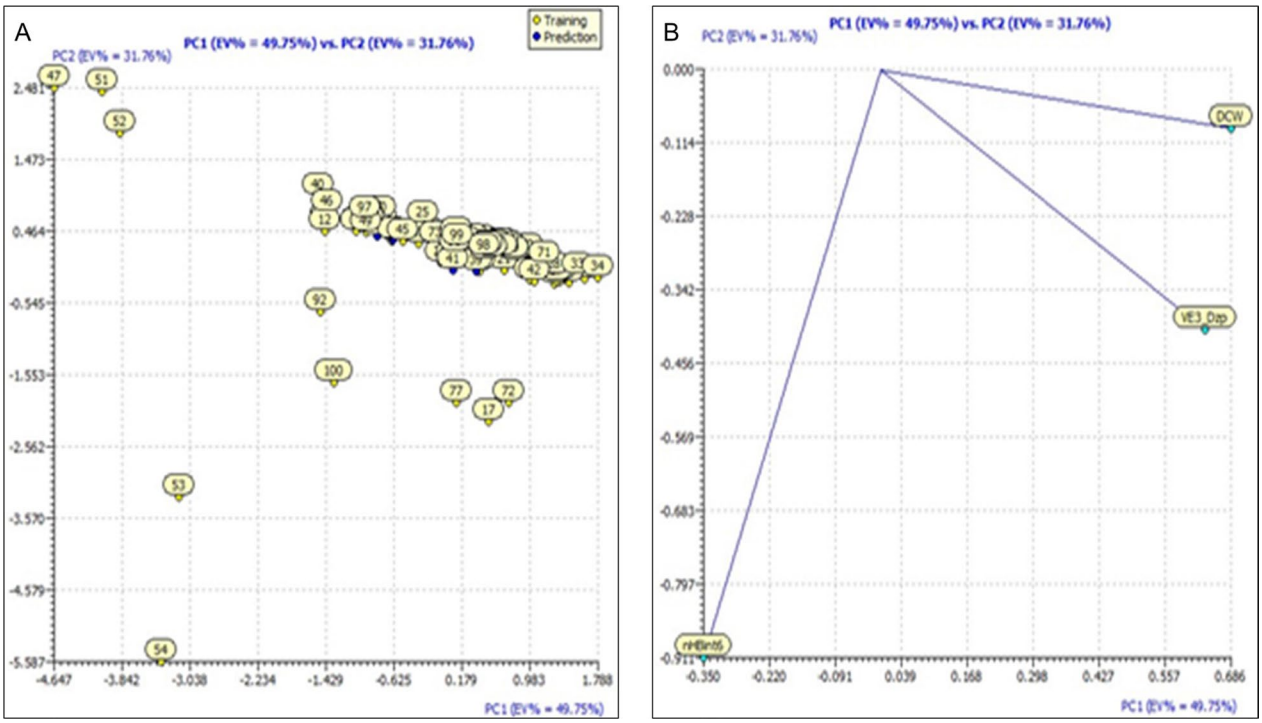

Fig. 1 PCA for QSAR model M-1; **A** Score plot for the M-1 descriptors; **B** Loading plot for the M-1 descriptors

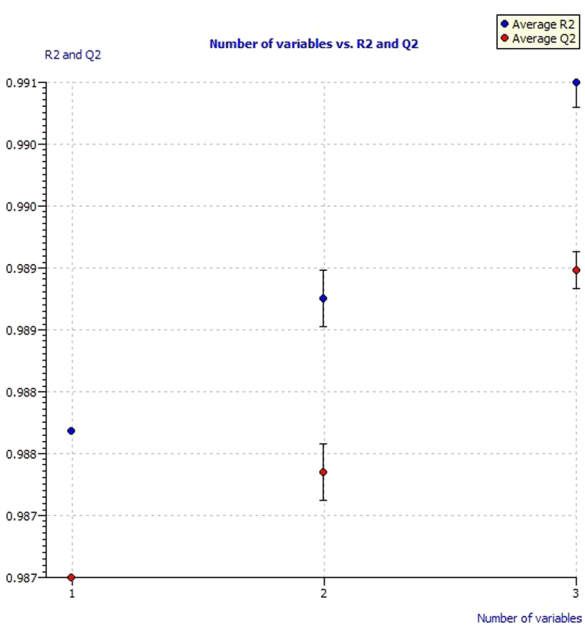

Fig. 2 Impact of inclusion of DCW on R2 and Q2 for M-1 training set

components. As evident from the score plot (Fig. 1A), very few dataset compounds were observed as outliers. The descriptor having maximum influence was observed to be nHBint6 followed by VE3_Dzp and DCW (Fig. 1B).

QSAR modeling and validation

Amazingly, a significant improvement (Fig. 2) in the values of R^2 and Q^2 for the training set was observed by including DCW. On that note, different 2D-QSAR models were built by including the single optimal descriptor. Models with best R^2 values for validation set were preferred for activity prediction. The QSAR equations of one-, two-, and three-descriptor models for best one-, two-, and three-descriptor models are reported in Table 1. The validated internal and external parameters for the best three models are represented in Tables 2 and 3, respectively. Table 4 represents statistical parameters for models M-1, M-2, and M-3.

All the models have higher R^2m values (˃ 0.5) and lower R^2m delta values (< 0.2) indicating stability and robustness. The values of the LOF and Friedman lack of fit (0.0001) [46] and *s* (0.007 to 0.0087) are very low which ensures that no over fitting is there in the models. Lower values for delta K and Kxx for model M-1 show good co-relation between descriptors and predicted responses with limited errors in computation [47, 48]. High R^2 adj values suggest convenient addition of a new descriptor to the model.

Model ID-1 with highest R^2 (coefficient of determination) has been evaluated as the best model satisfying the goodness-of-fit criteria and internal validation parameters. The scatter plot (Fig. 3A, B)

Table 1 Best 2D-QSAR models for PPARϒ receptor inhibitors

Model ID	Descriptor combination	QSAR equation
1	VE3_Dzp, nHBint6, DCW	$pIC_{50} = 0.0063 * nHBint6 - 0.0009 * VE3\_Dzp - 0.0084 * DCW + 7.7233$
11	GATS5v, DCW	$pIC_{50} = 0.0460 * GATS5v - 0.0086 * DCW + 7.6900$
21	DCW	$pIC_{50} = -0.0087 * DCW + 7.7442$

Table 2 Parameters for internal validation of best three models

Model ID	Q^2 LOO	R^2–Q2 LOO	RMSE cv	MAE cv	PRESS cv	CCC cv	Q^2 LMO	R^2Yscr	Q^2Yscr	RMSE AV Yscr
1	0.9894	0.0018	0.0081	0.0060	0.0057	0.9947	0.9886	0.0355	−0.0683	0.0771
11	0.9881	0.0014	0.0086	0.0064	0.0064	0.9940	0.9878	0.0231	−0.0483	0.0776
21	0.9868	0.0012	0.0090	0.0069	0.0071	0.9933	0.9865	0.0111	−0.0361	0.0781

Table 3 Parameters of external validation for the best three models

Model ID	RMSE ext:	MAE ext	PRESS ext	R^2ext	Q^2-F1	Q^2-F2	Q^2-F3	CCC ext	R^2m avg	R^2m delta
1	0.0053	0.0048	0.0004	0.9950	0.9927	0.9927	0.9955	0.9965	0.9500	0.0070
11	0.0051	0.0046	0.0003	0.9951	0.9932	0.9932	0.9958	0.9967	0.9593	0.0062
21	0.0063	0.0058	0.0005	0.9951	0.9894	0.9893	0.9935	0.9950	0.9307	0.0090

Table 4 Training set statistical parameters for best three models

Fitting criteria	Model1	Model 11	Model 21
R^2	0.9912	0.9895	0.9879
R^2adj	0.9909	0.9893	0.9878
R^2–R^2adj	0.0003	0.0002	0.0001
LOF	0.0001	0.0001	0.0001
Kxx	0.2541	0.3521	0.0000
Delta K	0.2064	0.2570	0.9940
RMSE tr	0.0074	0.0080	0.0086
MAE tr	0.0056	0.0061	0.0066
RSS tr	0.0047	0.0056	0.0065
CCC tr	0.9956	0.9947	0.9939
S	0.0076	0.0082	0.0087
F	3108.9384	3966.4605	6968.4382

clearly indicates a linearity in relationship among experimental and predicted values. The correlation between descriptors (x) and activity (y) were plotted with Kxy versus Q^2 LMO of the final model (model 1) (Fig. 4) displaying LMO parameter values are close enough to model parameters. It clearly states that the model is robust and stable. Y-scrambling tested the external validation parameters (Fig. 5). As the values of R^2Yscr and Q^2Yscr are very small, the models are believed to be good models and not the outcome of casual correlations.

Figure 6A, B shows the William's plots deciphering applicability domain of generated model (M-1).

Lower leverage values than threshold (h^* of 0.135) indicated that the training and test set molecules remained in the applicability domain of selected model as evident from the William's plot with 6 outliers only. Noticeably graph of insurbia (Fig. 7) resembled William's plot with same six outliers. This suggested that the selected model was best in terms of predicting experimental response. Additional file 1: Table S3 gives a comparative display of experimental and predicted IC_{50} values for the dataset compounds.

It clearly indicates that the descriptors (VE3_Dzp, nHBint6, and DCW) used to generate the best predictive model equation are not overfitting with the lowest LOF (0.0001) and high predictivity (Q^2LOO = 0.9894). It was also observed that the performance of model 3 build using a single optimal descriptor DCW was also impressive when compared with model 1. The performance of the models was evaluated by plotting the values of Q^2LOO and LOF (Fig. 8).

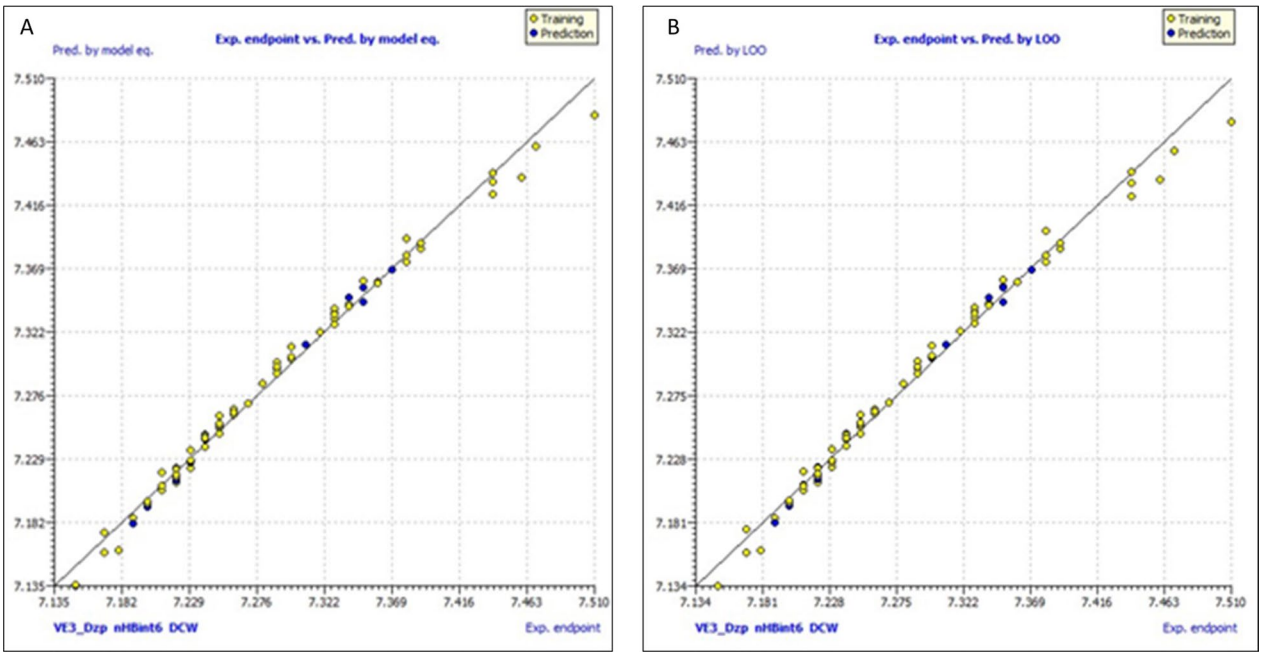

Fig. 3 Scatter plot of experimental pIC50 values versus predicted activity; **A** correlation between values predicted by model equation **B** correlation between the values calculated by LOO

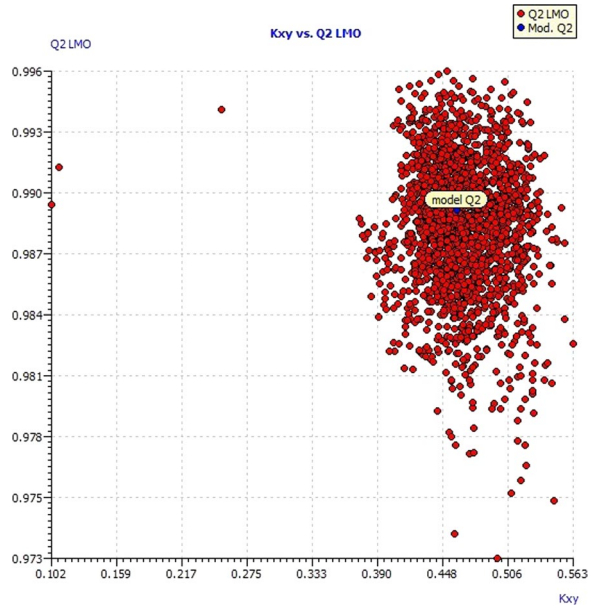

Fig. 4 Plot of Kxy versus Q2 LMO depicting correlation between computed variables (*x*) and predicted activity (*y*)

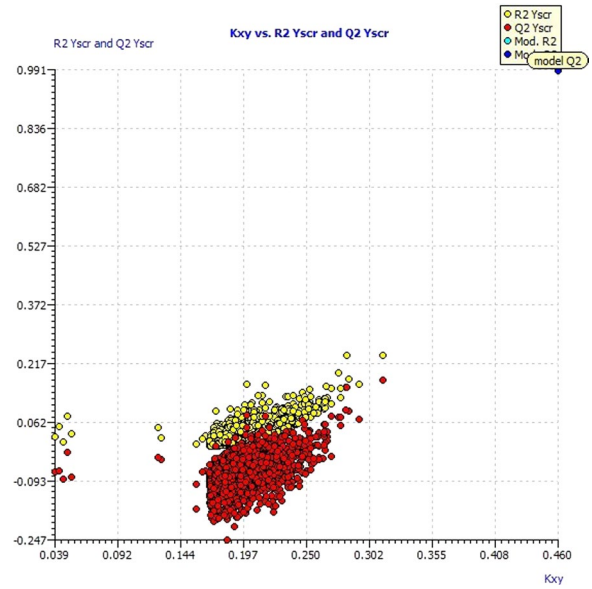

Fig. 5 Y-scramble plot depicting internal validation parameters

Predicted IC50 of topiramate–phenolic acid conjugates (TPAC)

The leverage values of all the designed molecules were observed to be below threshold leverage value ($h^* = 0.138$) suggesting the good applicability domain of the developed QSAR models. The predicted IC_{50} values of the designed compounds are displayed in Table 5. The highest inhibitory activity against PPARϒ was obtained for T3. The inhibitory activity reduced with the addition of (–OCH3) groups as evident from the pIC_{50} values of T4 and T10.

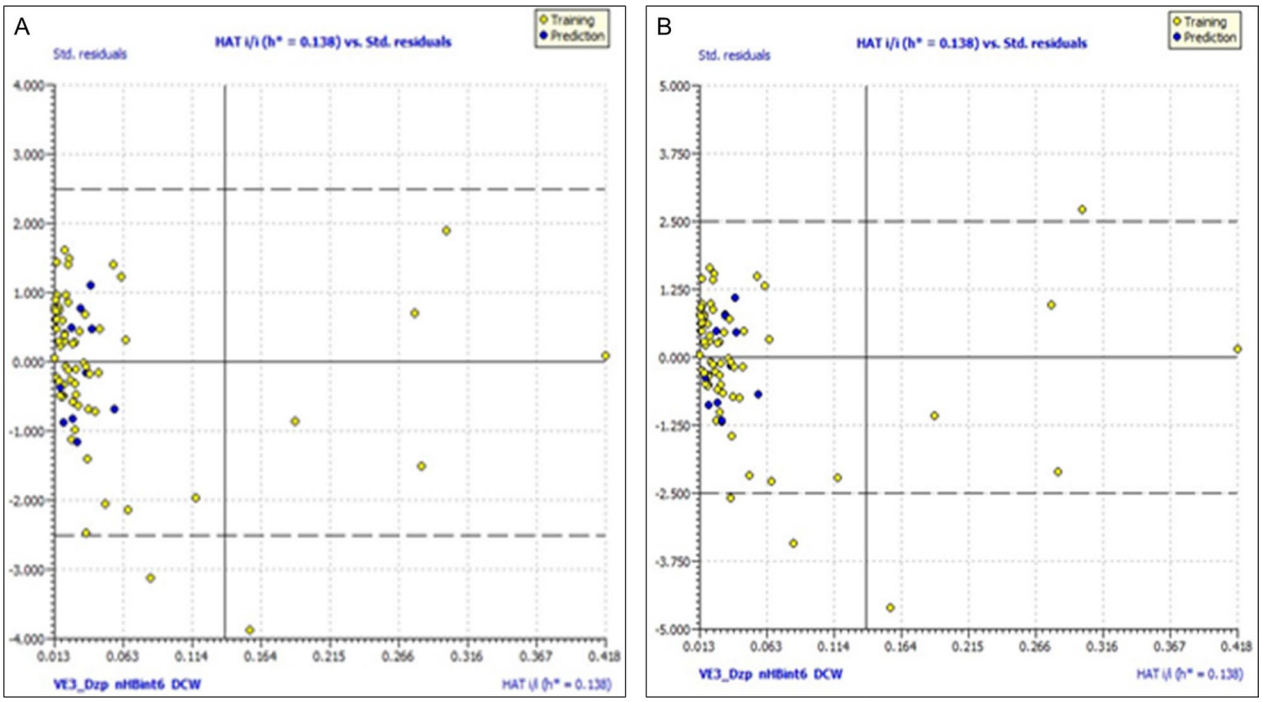

Fig. 6 William's plot for model (M-1) **A** HAT values vs standard residuals calculated from QSAR model equation; **B** HAT values versus standard residuals predicted by LOO

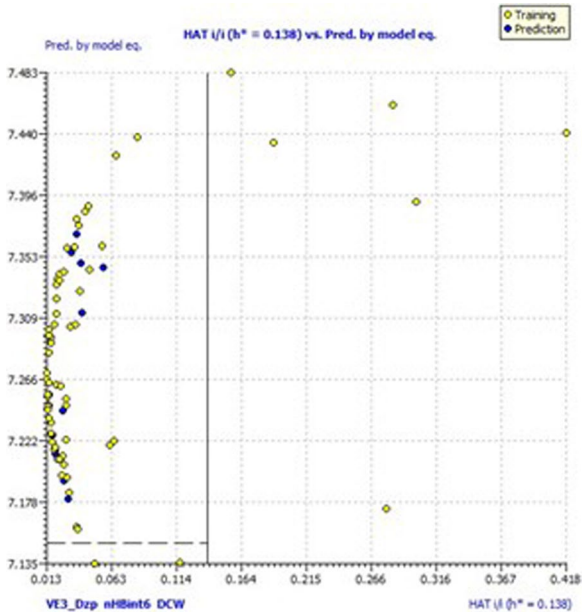

Fig. 7 The graph of insurbia

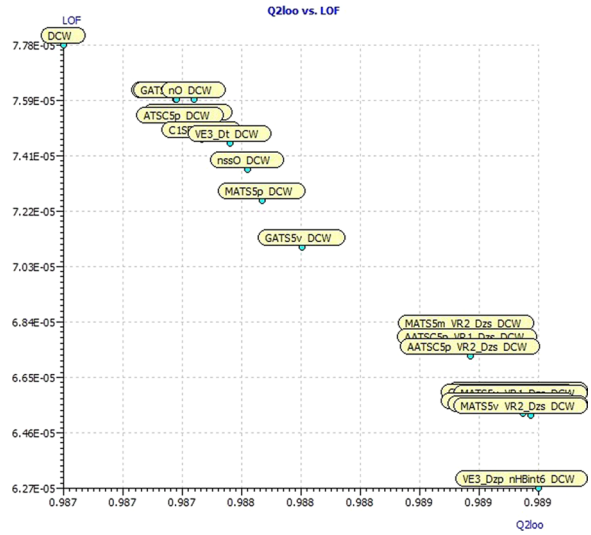

Fig. 8 Plot of Q2 LOO versus LOF

Table 5 Predicted pIC50 values of designed conjugates

Compound code	*R*	Predicted pIC_{50}
T1	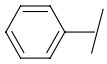	7.005003569
T2	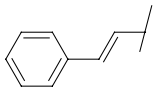	7.038592667
T3	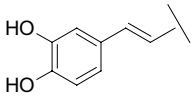	7.08435656
T4	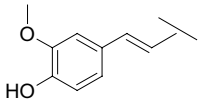	6.991701765
T5	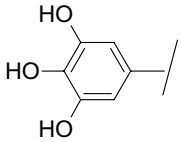	7.019504227
T6	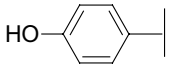	7.003357836
T7	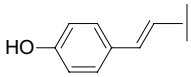	7.066946934
T8	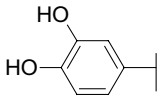	7.030767462
T9	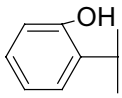	7.019279445
T10	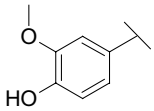	6.988112667

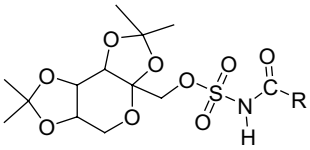

T1-T10

Mechanistic Interpretation

The designed 2D-QSAR model 1 was used for predicting the biological activity of the designed TPAC. According to the equation, the PPARϒ inhibitory activities are explained by three descriptors of the model equation which positively or negatively contribute to pIC_{50} values with respect to their regression coefficient values. The first descriptor VE3_Dzp is the logarithmic Randic-like eigenvector-based index from the Barysz matrix/weighted by polarizabilities and represents heteroatoms and multiple bonds in the molecules. The descriptor positively contributed toward the PPARϒ inhibitory potency [49]. In the designed conjugates, the presence of different electronegative atoms increases the polarization of carbon atoms that might increase the inhibition potency.

The next descriptor is nHBint6 which is an E-state descriptor and associated with electro-topological state of hydrogens establishing hydrogen bonds within a path length of six. The descriptor may also define intermolecular interactions having impact on biological and physic-chemical properties. The descriptor has a positive correlation with the pIC_{50} values [50]. We decipher that the presence of hydroxyl groups in the designed conjugates contributes positively toward the inhibition potencies. Interestingly, the inclusion of DCW (single optimal descriptor) generated best fitting models.

Molecular Docking Analysis

The open conformation of helix-12 is a prime requirement for co-repressor recruitment. The binding of an agonist to LBD within orthosteric pocket leads to a closed conformation, therefore recruiting co-activators and inducing transcription of PPAR*γ* genes. The important amino acid residues present within the orthosteric pocket are CYS285, SER289, HIS323, TYR327, LYS367, HIS449, and TYR 473, which play a major role in helix-12 folding [51]. Conclusively, it can be suggested that molecules interfering with proper folding of helix 12 around PPAR*γ*-LBD can be defined as PPAR*γ* antagonists [52]. Further, ligands binding to the allosteric site within the PPAR*γ*-LBD do not display any competition with classical agonistic ligands for binding at orthosteric site The amino acid residues present within allosteric acid are GLU259, LYS265, HIS266, ARG288, SER289, GLU295, SER342, GLU343, and LYS367 which significantly interfere with helix-12 folding [21]. Therefore, PPAR*γ* antagonists can be designed according to the helix12-folding inhibition hypothesis.

The binding interactions of the designed conjugates (T1–T10) along with CF, TPM, and GW9662 with crystal structure of PPARγ (PDB ID: 3VSO) are displayed in Table 6. Among the 10 designed conjugates, T3 shows stable and strong interactions with the receptor. The designed ligand binds to an alternate site/allosteric site within the ligand binding domain of the crystal structure of PPAR*γ*. The intramolecular hydrogen bonding interactions between the allosteric

Table 6 Binding affinities and interactions of TPAC with amino acid residues

Conjugates	Binding energies (Kcal/mol)	Interactions with amino acids	
		Hydrogen bonds	Hydrophobic interactions
T1	−9.0	ARG288, GLU343	SER342, ILE281, LEU330, CYS285, ARG288
T2	−10.84	SER289, CYS285	HIS449, TYR327, LEU469, HIS323, ARG288, ALA292, ILE326, LEU330, ILE281, LEU336, MET364
T3	−11.27	ARG288, CYS285, MET364, PHE360	MET329, ILE326, LEU330, LEU333, TYR327, CYS285
T4	−11.14	ARG288, CYS285, PHE360, PHE363	MET329, ILE326, LEU330, LEU333, TYR327, CYS285, ARG288, LEU356, PHE363, MET364, ILE281, LEU353
T5	−9.34	SER342, LEU340	LEU255, ARG280, ILE281, MET348, CYS285, GLY284, ARG288, VAL339, ILE341, PHE264
T6	−9.13	ARG288, GLY284, GLU343	ILE341, MET348, LEU330, ILE281, CYS285, ARG288
T7	−10.56	ARG288, CYS285, PHE360	ALA292, MET329, ILE326, LEU330, LEU333, TYR327, ILE281, LEU353, MET364, CYS285
T8	−10.36	ARG288, CYS285, PHE360	ALA292, MET364, ILE326, LEU330, LEU333, TYR327, LYS367, ILE281, LEU353, MET364, CYS285
T9	−9.37	ARG288, GLU343	MET364, ILE326, LEU330, LEU353, PHE287
T10	−10.40	CYS285, PHE360, PHE363	ILE326, MET329, LEU330, LEU333, ARG288, TYR327, MET364, CYS285, LYS367, ILE281, LEU353
TPM	−6.9	ARG280	CYS285, ARG288, PHE264, PHE287, LEU330, VAL339, LEU340, MET364
CF	−6.1	CYS285	ARG288, SER289, ALA292, ILE326, MET329, LEU330, LEU333
GW9662	−9.0	ARG288, ILE326, TYR327	CYS285, SER289, ALA292, ILE296, HIS323, MET329, LEU330, LEU333, MET364, LYS367, HIS449

pocket residues (ARG288, CYS285, MET364, and PHE360) and T3 might destabilize the helix-12.

It is evident that there are no interactions of T3 with residues that are involved in proper folding of helix-12 (SER289, HIS323, TYR327, LYS367, HIS449, and TYR473) within the orthosteric pocket of PPARγ ligand binding domain. Also, hydrophobic interactions (MET329, ILE326, LEU330, LEU333, TYR327, and CYS285) might displace the helix-12 from position thereby disfavoring transcriptional process (Fig. 10). Moreover, it was interesting to see that the designed conjugate T3 showed stronger interactions with the allosteric pocket residues than the parent pharmacophores (Fig. 9), CF (binding affinity, −6.1 kcal/mol) and TPM (binding affinity, −6.9 kcal/mol) respectively. Similarly, T3 formed stronger interactions with the allosteric pocket residues when compared to the irreversible PPARγ antagonist, GW9662 (binding affinity, −9.0 kcal/mol) (Fig. 9).

For designing potential PPARγ antagonists, it might be imperative to sustain H-bond interactions with ARG288, SER342, LYS367 and HIS449 within allosteric pocket in the LBD [53]. Moreover, hydrophobic interactions with allosteric site residues PHE282, ILE281, LEU356, TYR327, ILE326, LEU330 and MET348 that can destabilize the H12 contribute to inhibition potency of ligands [44, 54, 55].

Molecular dynamic simulation

The molecular dynamics-based studies revealed the deep understanding of protein ligand interactions over a period of time. The interaction energies of PPARγ-CF complex, PPARγ-TPM complex and PPARγ-T3 complex in a neutralized system are given in Table 7.

From the above data (Table 7), it was clear that all the protein–ligand complexes were quite stable within the solvent medium. Of all the three PPARγ-ligand complexes, PPARγ-T3 complex exhibited lowest potential energy (Fig. 10). Lower the potential energy, higher are the attractive force between the protein and ligand molecule. It was therefore confirmed that PPARγ-T3 complex was most stable with strong intermolecular attractions (also refer Additional file 1: supplementary data Figs. 1S, 2S, and 3S).

The complex revealed high fluctuation rate during the MD simulation study as total 0 to 100 ns RMSD (Fig. 11A). Initially at 0 ns the starting point the protein ligand deflected to ~ 4 Å. From 5 nanoseconds onward, the ligand was observed to be high in fluctuation reaching upto a ~ 9 Å with respect to the protein movement. The protein structure was almost a constant at around ~ 3 Å. From 35 nanoseconds to 60 ns and from 61 to nearly 85 nanoseconds, the ligand fluctuation trend was almost similar in a span of 25 nanoseconds where the ligand aroused from ~ 1 Å

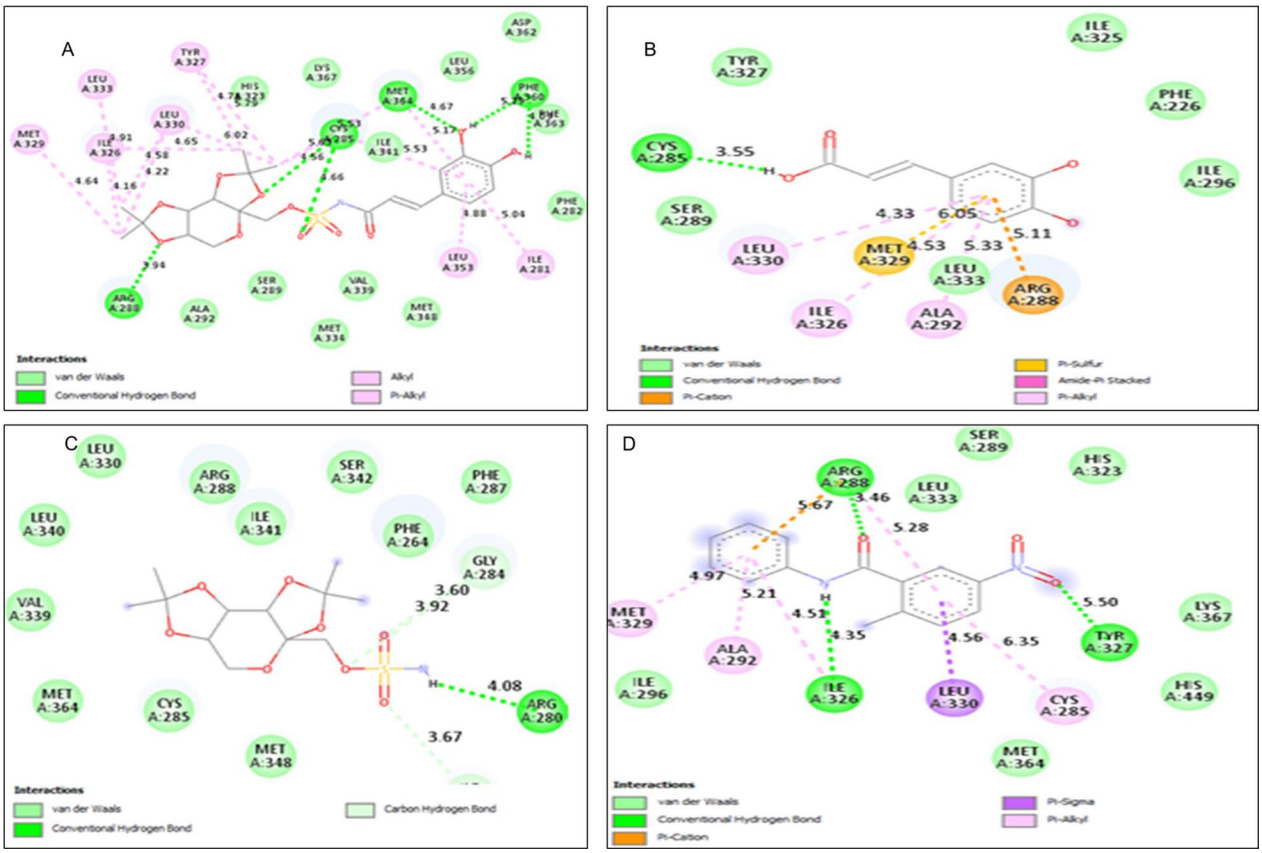

Fig. 9 Binding interactions at allosteric site of PPARγ LBD (PDB ID: 3VSO) with **A** T3 **B** CF **C** TPM **D** GW9662 (irreversible PPARγ antagonist)

Table 7 Dynamic properties of PPARγ-caffeic acid complex, PPARγ-topiramate complex, and PPARγ-T3 complex

Type of energy	PPARγ-caffeic acid complex	PPARγ-topiramate complex	PPARγ-T3 complex
Bond average energy	1283.25 kJ/mol	1385.02 kJ/mol	1312.6 kJ/mol
Potential energy	−7.3257912*e*+05 kJ/mol	−7.2699112*e*+05 kJ/mol	−7.3615656e+05 kJ/mol
Proper-Dihedral average energy	10,561.9 kJ/mol	10,664.8 kJ/mol	10,716.3 kJ/mol
Improper-Dihedral average energy	179.937 kJ/mol	189.107 kJ/mol	185.199 kJ/mol

and going upto ~ 9 Å. Finally, from 85th nanosecond onward the ligand bounded within the protein fluctuation within the range of ~ 0.7 Å to ~ 2.5 Å (Fig. 11A). The PPARγ-TPM complex revealed an acceptable fluctuation rate during the MD simulation study as total 0 to 100 ns RMSD (Refer Additional file 1: Fig. S5). Initially, at 0 ns the starting point the protein ligand deflected to ~ 0.35 Å. From 5 nanoseconds onward, the ligand was observed to be high in fluctuation reaching upto a ~ 9 Å with respect to the protein movement. The protein structure was almost a constant at around ~ 0.3 Å. From 0 to 15 ns, it went to ascending order upto ~ 0.3 Å, and 15 ns onward it is constant upto 100 nanoseconds with ~ 0.3 Å. The ligand initially aroused ~ 0. ~ 45 Å by 20 nanoseconds and later constant fluctuation is observed in a range of ~ 0.3 to 0.325 Å till 100 nanoseconds. At the 100 nanosecond, the binding affinity of TPM and PPAR-γ was found out to be −4.98299*e*+05 kJ/mol (Fig. 11B).

Similarly, the PPARγ-T3 complex revealed an acceptable fluctuation rate during the MD simulation study as total 0 to 100 ns RMSD. Initially, at 0 ns the starting point the protein deflected from 0.18 Å to max ~ 0.28 Å and finally settled at ~ 0.25 Å to 100 nanoseconds, whereas the ligand from 0 nanosecond deflected to ~ 0.32 Å and reached upto ~ 0.57 Å at 100 nanoseconds (Fig. 11C).

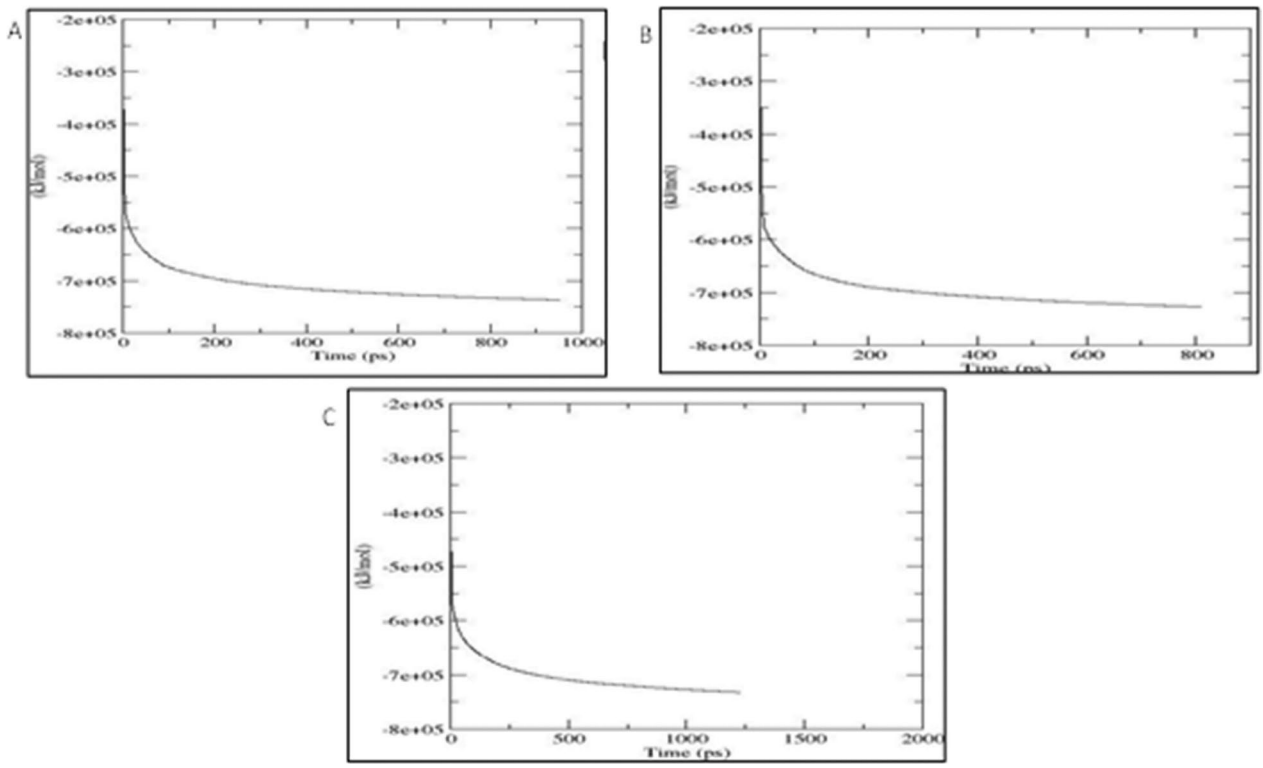

Fig. 10 Decrease in potential energy with respect to time; **A** PPARγ-CF complex **B** PPARγ-TPM complex **C** PPARγ-T3 complex

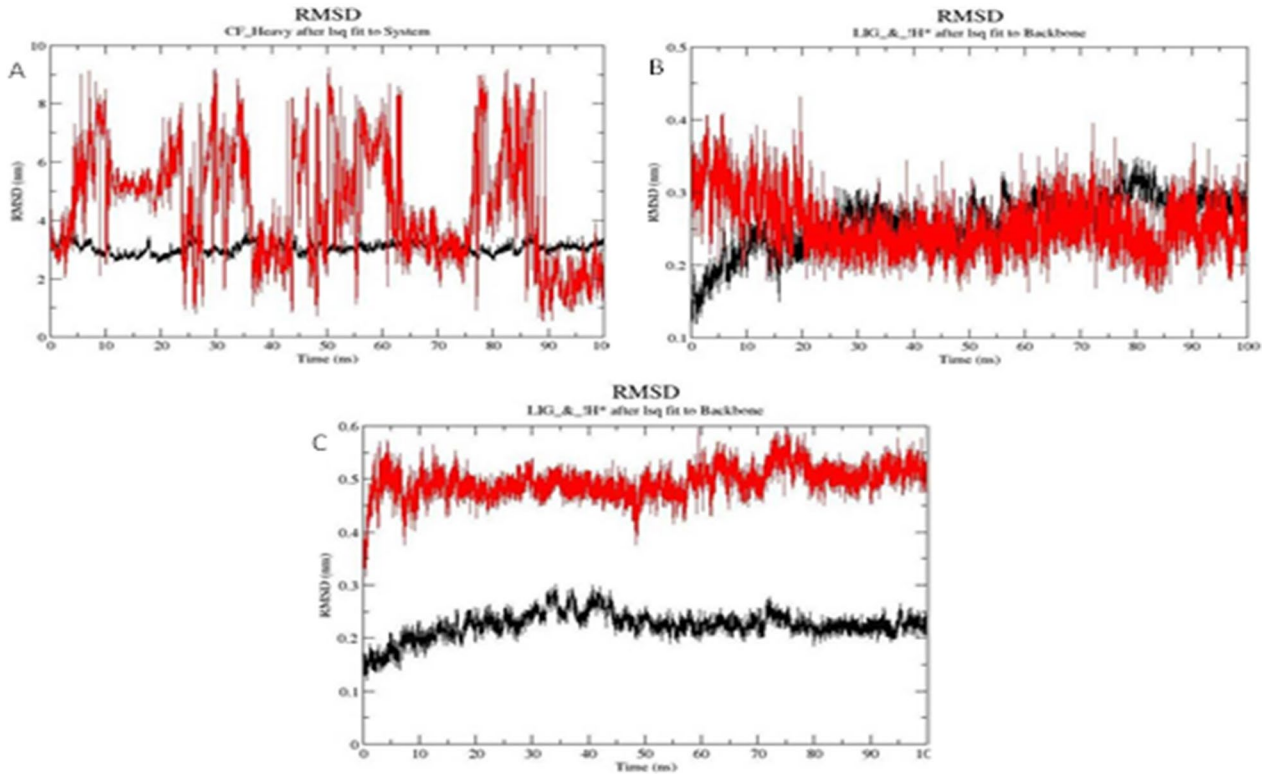

Fig. 11 RMSD analysis of PPARγ-ligand complex; **A** PPARγ-CF complex **B** PPARγ-TPM complex **C** PPARγ-T3 complex

The root mean square fluctuation (RMSF) calculates mean fluctuations atoms or amino acid residues during the entire MD simulation period. For PPARγ-CF complex, the calculated RMSF for the protein region is a maximum 0.5 Å and the ligand (CF) reached up to 0.15 Å (Fig. 12A). For PPARγ-TPM complex, the calculated RMSF for the protein region is a maximum 0.75 Å and the ligand (TPM) reached up to 0.17 Å (Fig. 12B). Also the calculated RMSF for the protein region (PPARγ-T3 complex) is a maximum 0.75 Å and the ligand (T3) reached up to Å 0.18 (Fig. 12C). The calculated RMSF values below 1 Å reveal no higher fluctuations within the atoms of the complexes, suggesting that all the PPARγ-ligand complexes were stable.

Rg (radius of gyration) analysis explains the extent of unfolding and folding of the protein–ligand complex during entire MD simulation. The compactness of protein and bound ligand can be defined by Rg. High Rg values indicate lower compactness of proteins and ligand thereby suggesting poorly bound complex and vice versa. Here in PPARγ-CF complex, the protein PPAR-γ exhibited a maximum of 2 nm and ligand CF exhibited at very low nearly 0.3 nm of fluctuation in Rg (Fig. 13A). In case of PPARγ-TPM complex, the protein PPAR-γ exhibited a maximum 2 nm and TPM exhibited at very low nearly 0.47 nm of fluctuation in Rg (Fig. 13B), while in case of the PPARγ-T3 complex, protein PPAR-γ exhibits a maximum 2 nm and ligand (T3) exhibited at very low as started with 0.5 nm and reduced to 0.2 nm of fluctuation in Rg revealing a highest stability in contrast to the complex (Fig. 13C).

In the process of drug design, h-bonds play a vital role in absorption, metabolism, and transportation too. The PPAR-γ and CF complex revealed significant change in the bonding parameter, where initially the ligand was interacting within the binding site region 3 and maximum 4 h-bonds. Finally, from the 90 ns to 100 ns the number of h-bonds is only 1 with an energy of −4.98780*e*+05 kJ/mol (Fig. 14 A). TPM was observed to interact within the binding site region with maximum 7 h-bonds at nearly ~ 30 and ~ 70 ns. Finally, from the 80 ns to 100 ns the number of h-bonds is acquainted

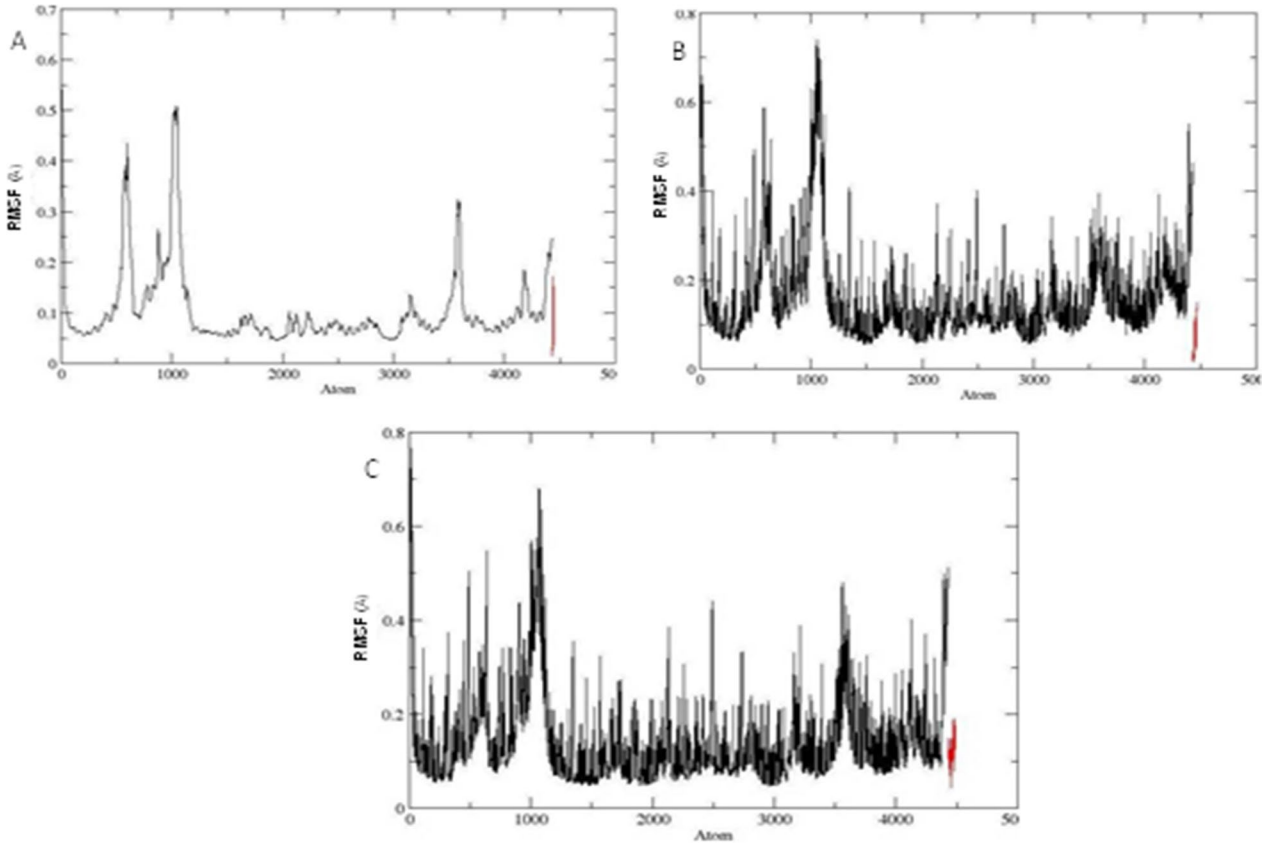

Fig. 12 RMSF analysis of PPARγ-ligand complex; **A** PPARγ-CF complex **B** PPARγ-TPM complex **C** PPARγ-T3 complex

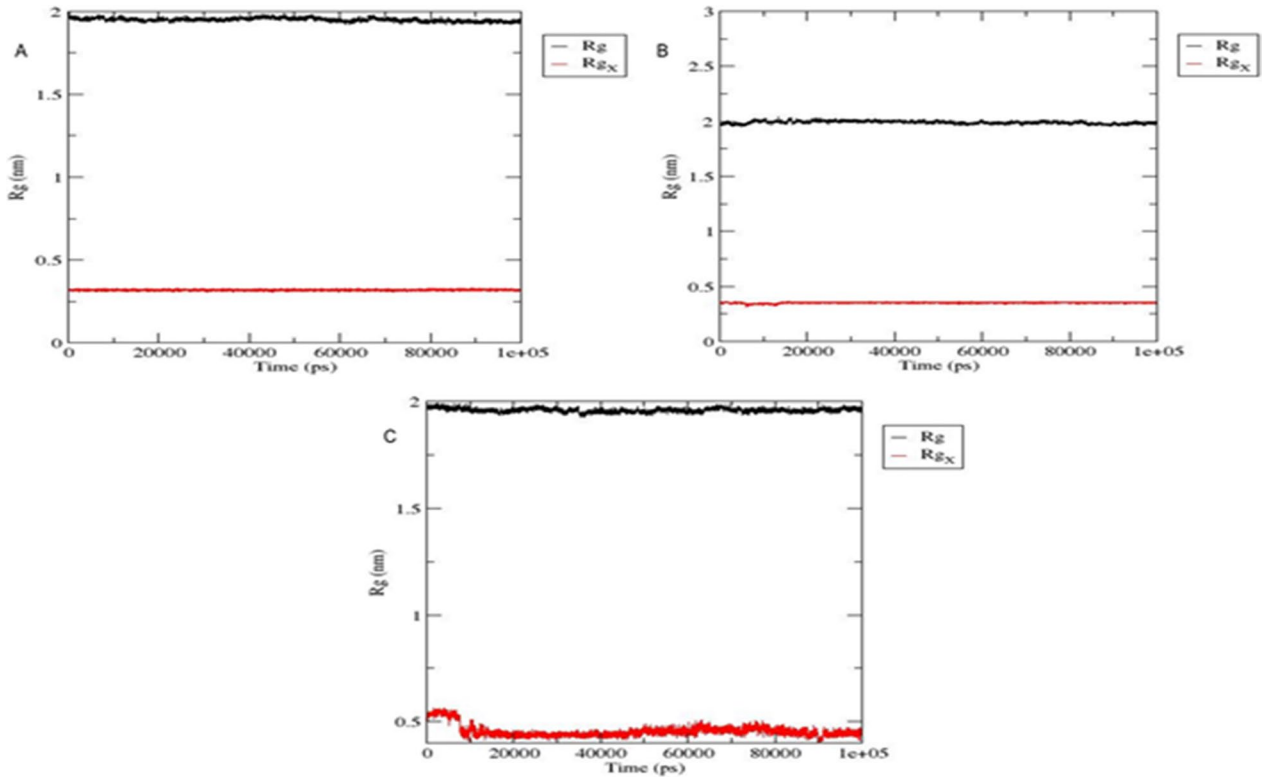

Fig. 13 Radius of gyration data for PPARγ-ligand complex; **A** PPARγ-CF complex **B** PPARγ-TPM complex **C** PPARγ-T3 complex

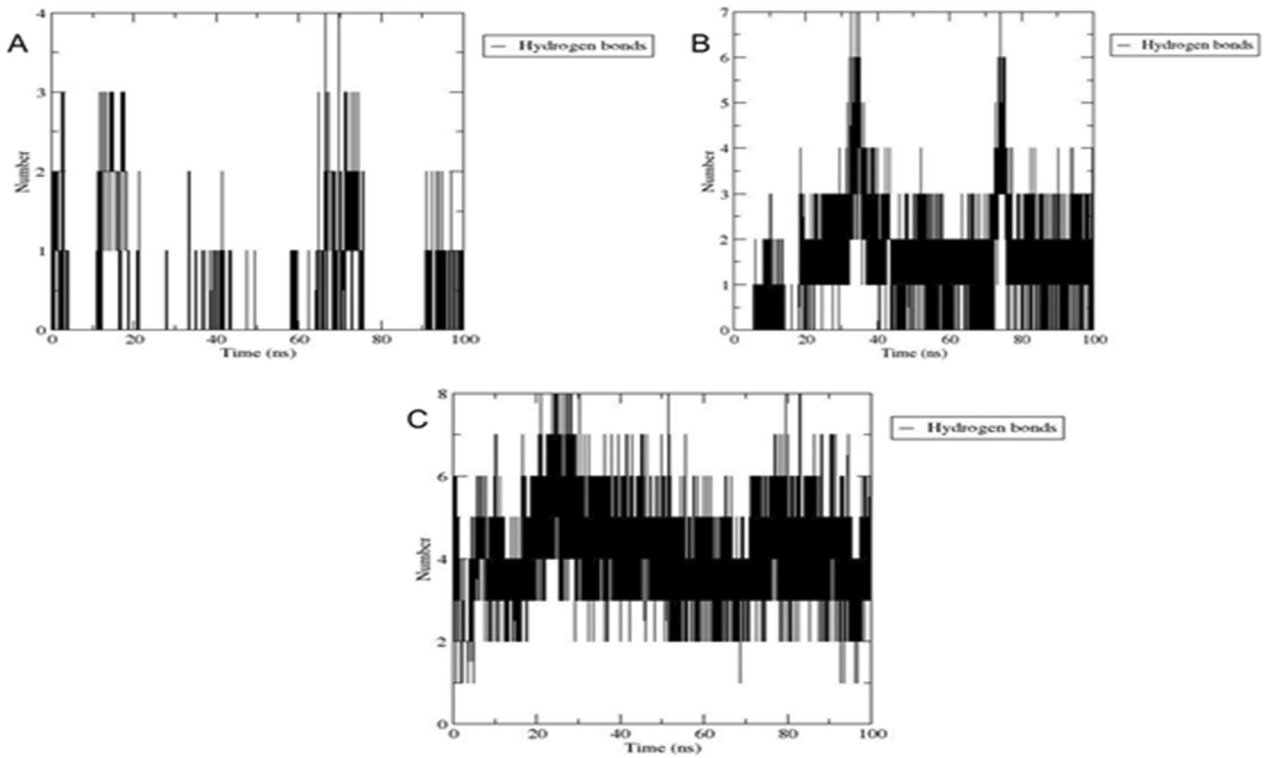

Fig. 14 Hydrogen bond interactions in PPARγ-ligand complex; **A** PPARγ-CF complex **B** PPARγ-TPM complex **C** PPARγ-T3 complex

to 2 and 3 (Fig. 14B). T3 was observed to interact within the with maximum 8 h-bonds at between ~ 20 and ~ 30 ns at 50 ns, and between 75 to 80 ns. At nearly 100 ns, the number of h-bonds is acquainted to 5 and 6 with an energy of $-4.99215e+05$ kJ/mol (Fig. 14 C).

SASA (solvent of accessible surface area) detects changes in conformations in the protein–ligand complex that can be assessed by water or solvent during entire MD simulation. In our study, the black line/graph indicates the protein in solvent system and red lines graph indicates the protein and ligand complex for the entire length of time period of MD simulation. The overlapping exhibits that there are no or very minor fluctuations and the entire system is stable. However, lower deviation (by 155 nm^2) was observed for PPARγ-T3 complex in comparison to PPARγ-CF and PPARγ-TPM complexes with a deviation by 160 nm^2 and 165 nm^2, respectively (Fig. 16), indicating higher stability of PPARγ-T3 complex (Fig. 15).

The molecular docking and MD simulations clearly suggested that in contrast to individual pharmacophores the conjugate T3 would strongly bind to allosteric site within the LBD of PPARγ, thereby acting as an antagonist.

Chemistry

Synthesis of T3 [3-(3,4-Dihydroxy-phenyl)-acryloyl]-sulfamic acid 2,2,7,7-tetramethyl-tetrahydro-bis[1,3] dioxolo[4,5-b;4′,5′-d]pyran-3a-ylmethyl ester

Buff yellowish crystalline solid; Yield (53%); mp (175 °C); IR (KBr, cm^{-1}): 3700 (NH, amide) 3400 (–OH, phenolic) 1353, 1252 ($-CH_3$) 1645–1630 (C=O, amide), 1600–1445 (C–C), 1070 (C–O),1379, 1342 (S=O), 978 (trans alkene); ^{1}H NMR (400 MHz, DMSO-d 6): δ 1.29–1.47 (12H, 1.29(s), 1.34 (s), 1.37 (s), 1.47 (s)), 3.63 (1H, *d*, *J*=7.6 Hz), 3.74 (1H, *d*, *J*=7.6, Hz), 3.98 (2H, *d*, *J*=2.6 Hz)), 4.03 (1H, dd, *J*=12.9, 2.6 Hz), 4.25 (1H, dd, *J*=12.9, 3.0 Hz), 4.77–4.87 (2H, 4.60 (s), 4.62 (s)), 6.186 (1H, *d*, *J*=15.7 Hz), 6.78 (1H, *d*, *J*=8.4 Hz)), 6.95 (1H, *d*, *J*=1.9 Hz), 7.08 (2H, (dd, *J*=8.4, 1.9 Hz), 7.43 (IH, *d*, *J*=15.7 Hz), 7.61 (1H, *s*). 13 C NMR (100 MHz, DMSO-d 6): δ 26.3–26.4 (4C, 26.3 (*s*), 26.1 (*s*), 25.1 (*s*), 24.2 (*s*)), 65.4 (1C, *s*), 60.7 (1C, *s*), 69.17 (1C, *s*), 69.9 (1C, *s*), 70.1 (1C, *s*), 70.41 (1C, *s*), 100.9 (1C, *s*), 108.0 (1C, *s*), 115.05 (1C, *s*), 115.8 (1C, *s*), 116.0 (1C, *s*), 121.4 (1C, *s*), 125.7 (1C, *s*), 145.7 (1C, *s*), 146.8 (1C, *s*), 148.5 (1C, *s*), 168.47 (1C, *s*).

As depicted in Scheme 1, T3 was synthesized by coupling of topiramate to caffeic acid using DCC and

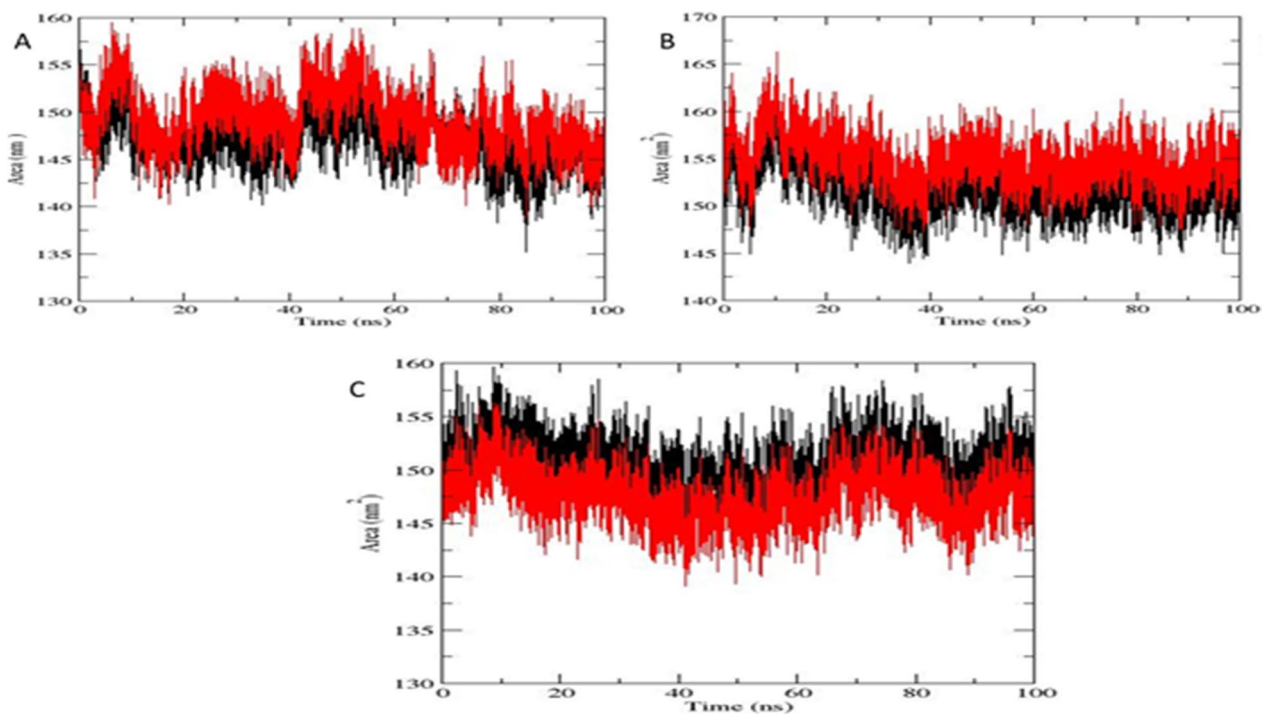

Fig. 15 SASA analysis for PPARγ-ligand complexes **A** Black line—SASA (PPAR-γ) and Redline—SASA for Protein and Ligand (PPARγ-CF); **B** Black line—SASA (PPAR-γ) and Redline—SASA for Protein and Ligand (PPARγ-TPM); **C** Black line—SASA (PPAR-γ) and Redline—SASA for Protein and Ligand (PPARγ-T3)

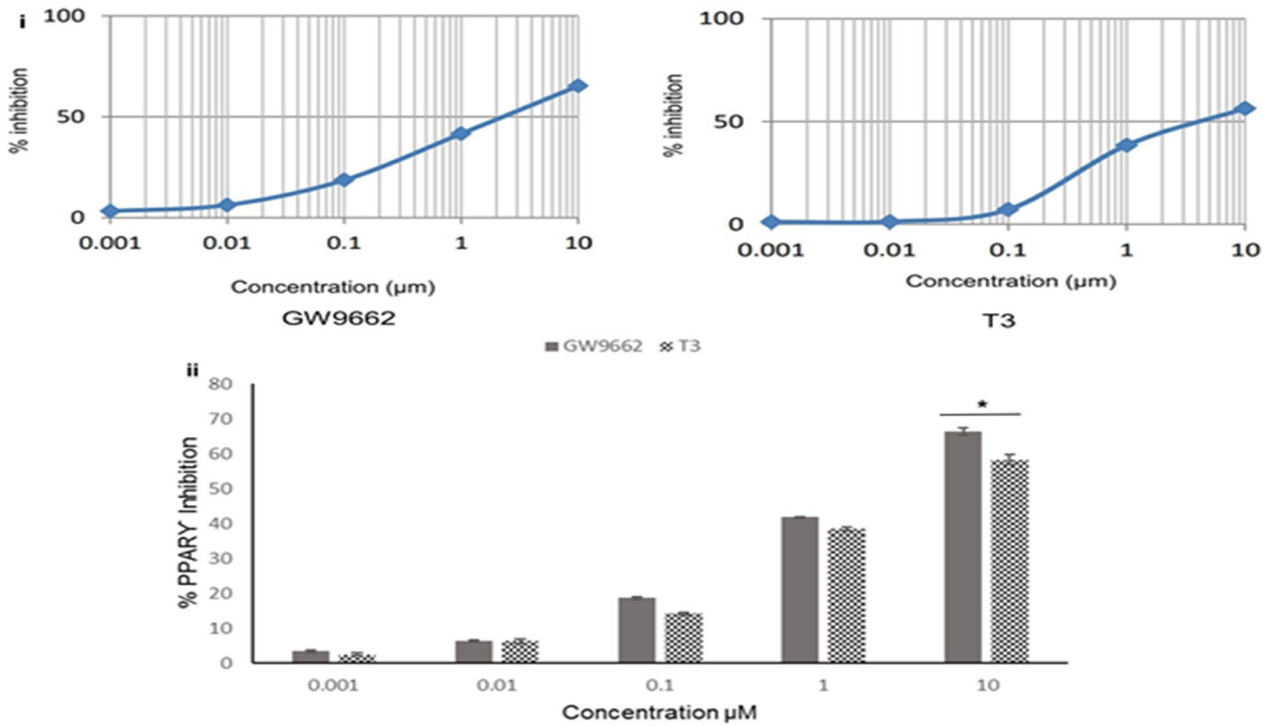

Fig. 16 **i** Dose-dependent inhibitions of PPARγ by GW9662 and T3 **ii** % PPARγ inhibition T3 relative to GW9662 [data given in terms of mean ± standard deviation (*$p < 0.05$) at $n = 3$ experiments]

catalytic amount of DMAP. Initially caffeic acid (1 equivalent) and DCC (1.1 equivalent) were dissolved in sufficient of ice cold DMF and stirred for one hour on a magnetic stirrer. The reaction proceeds with formation of acylimminium ion intermediate. DMAP acts as a acyl transfer reagent. After one hour of stirring, topiramate (2 equivalent) dissolved in excess DMF was added to the above reaction mixture and stirred continuously for 48 h. Structure of the synthesized conjugate was characterized using IR, NMR (^{1}H and ^{13}C). In IR spectra characteristic peaks 3700 (NH amide), 3400 (–OH, phenolic) 1353, 1252 (–CH_3) 1645–1630 (C=O, amide carbonyl), 1600–1445 (C–C), 1379, 1342 (S=O), and 978 (trans alkene) were confirmed. Further, in ^{13}C NMR spectra carbons of amide carbonyl functionality were confirmed at 167–170 ppm (please refer Additional file 1: Figs. S4 and S5) [56].

Pharmacological studies

Enzyme inhibition assay

For evaluating T3 as a PPARγ inhibitor, TR-FRET co-activator assay was conducted. Binding of an agonist like rosiglitazone to PPARγ, causes a conformational change around helix 12 in LBD that increases the affinity of co-activator peptide. Upon excitation at 337 nM, energy is transferred to the fluorescein label on co-activator peptide from the europium label, therefore detected as emission. In agonistic mode, the T3 did not display any significant increase in fluorescence emission even at 10 µmol/L. On the other hand, in the antagonist mode, T3 antagonized agonist (rosiglitazone) induced fluorescence responses. From Fig. 16 it is quite evident that both GW9662 ($IC_{50} = 4.49$ µM) and T3 ($IC_{50} = 7.45$ µM) exhibited dose-dependent inhibition of PPARγ.

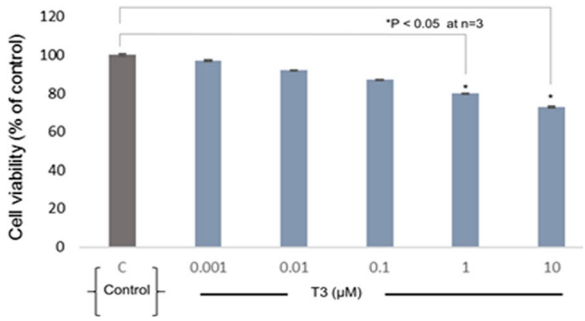

Fig. 17 Effect of T3 on 3T3-L1 preadipocytes [Values presented as mean ± standard deviation (*$p < 0.05$) at $n = 3$ experimental repeats]

Effect of T3 on 3T3-L1 preadipocytes viability

For examining the cell level toxicity, the 3T3-L1 preadipocytes were treated with range of T3 concentrations (0.001, 0.01, 0.1, 1 and 10 μM) for 72 h and cell viability was assessed by MTT assay. Up to 0.1 μM of T3, no significant reduction in viability with respect to control (untreated) of 3T3-L1 preadipocytes were observed. A reduction in cell viability of about 10% and 20% was observed (Fig. 17) for 1 and 10 μM of T3 ($p < 0.05$, ANOVA with t-test). Based on the above observations, concentrations below 10 μM (1, 3, 5. 7 and 10) of T3 were selected to evaluate the percentage lipid accumulation. The values for percentage viability of 3T3-L1 preadipocytes are provided (mean ± standard deviation) corresponding to triplicate experiments.

Effect of T3 on 3T3-L1 lipid accumulation and adipocyte differentiation

Oil Red O staining method explored the percentage of intracellular lipid accumulation in adipocyte stem cells. A dose-dependent inhibition of 3T3-L1 cells by T3 was observed. From the microscopic examinations it was pretty evident that there is reduction in size and number of 3T3-L1 cells containing larger lipid droplets (indicated in yellow colored arrows) with respect to control group (Fig. 18i). The percentage of fat accumulation was considerably reduced in T3 5–7 μM and highest at 10 μM concentrations (Fig. 18ii), with IC_{50} calculated as 7.98 μM.

Effect of T3 on 3T3-L1 on PPARγ expression

It was very evident that reduction in lipid accumulation was very significant in the cell groups treated with 10 μM. For evaluating T3 as downregulator of PPARγ expression (master regulator of adipogenesis and differentiation), western blot was performed. T3 (10 μM) significantly decreased PPARγ expression in 3T3-L1 cells in comparison normal control (untreated) and GW9662 (10 μM) as positive control. These results were specific because β-actin levels were not affected (Fig. 19).

Conclusion

Drug conjugates display better pharmacological properties than their individual pharmacophores. We synthesized novel drug conjugate TPAC as PPARγ inhibitors. PPARγ majorly orchestrates adipose tissue differentiation [57]. The development of new antiobesity medications has now centered around targeting adipogenesis and thereby associated signaling molecules and transcription factors. On this context, PPARγ becomes a promising target for antiobesity molecules. Topiramate, a marketed anticonvulsant drug, has been successfully repurposed and used as an antiobesity drug. Essentially, topiramate is a carbonic anhydrase inhibitor that tends to control obesity through enhancing satiety and regulating lipid metabolism. The antiobesity potential of the phenolic acids is attributed to controlling gut microbiome, energy metabolism, and control of adipogenic signaling

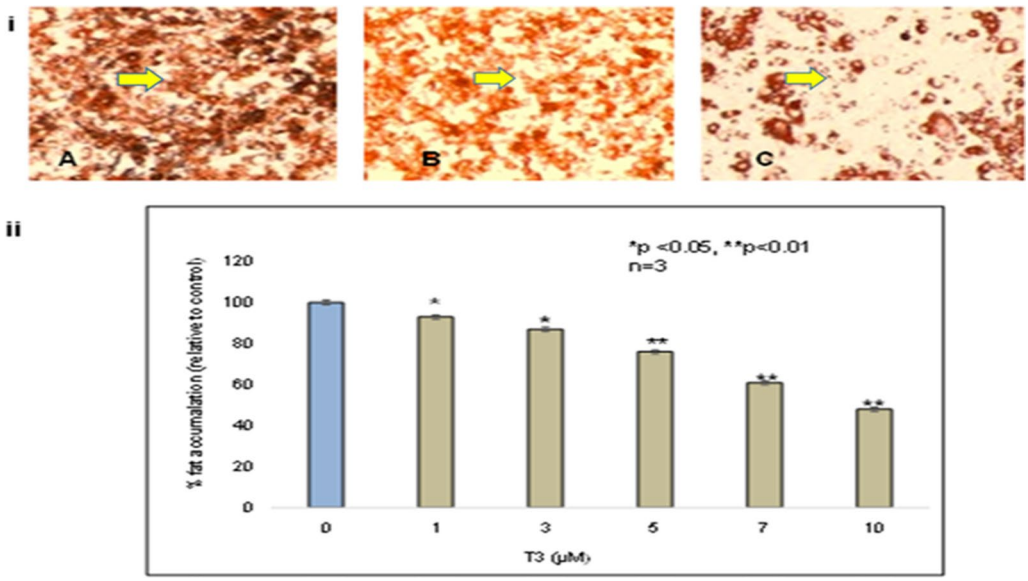

Fig. 18 Effect of T3 on lipid accumulation on 3T3-L1 preadipocytes **i** (A) control; (B) T3 (5 μM); (B) T3 (10 μM). **ii** Percentage fat accumulation. All the values are expressed as mean ± SD, at $n = 3$ biological repeats

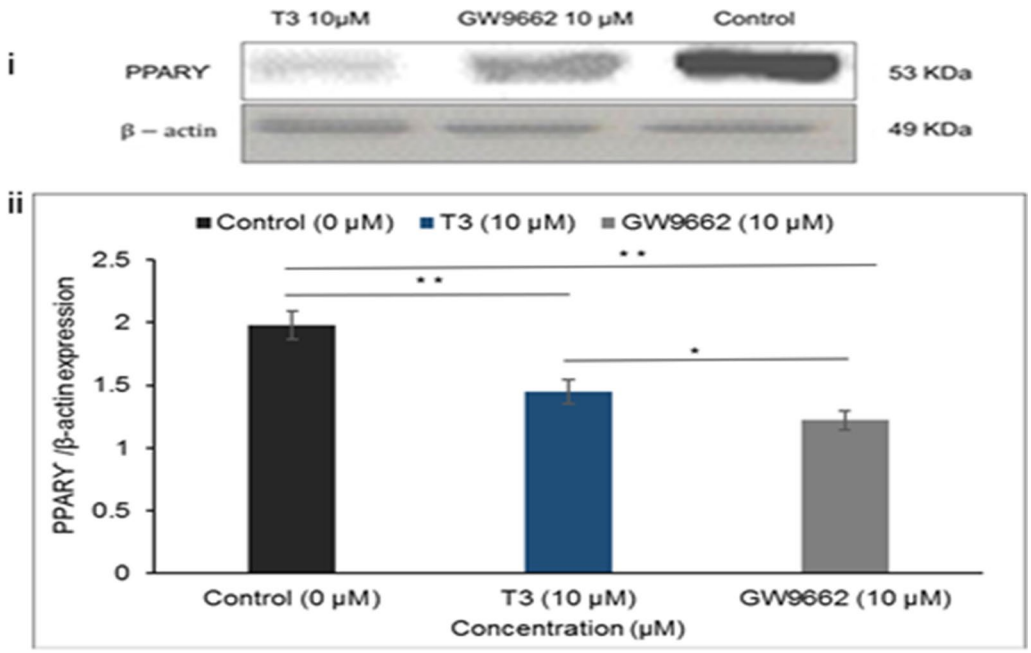

Fig. 19 Effect of T3 on 3T3-L1 preadipocytes PPARγ expression (**i**) comparative downregulation of PPARϒ expressions of T3 with respect to positive control GW9662 and normal control (untreated 3T3-L1 cells) (**ii**) PPARϒ expressions of T3, positive control GW9662 and normal control (untreated 3T3-L1 cells) relative to β-actin. The values are expressed as mean ± standard deviation for $n = 3$ biological repeats (*$p < 0.05$ and **$p < 0.01$)

pathways. On such grounds, it was interesting to design a new conjugate with two distinct pharmacophores exhibiting antiobesity potential via targeting adipogenesis and subsequently PPARγ.

To summarize, 10 topiramate–phenolic acid conjugates were designed and their PPARγ inhibitory activities were predicted by robust 2D QSAR model with excellent goodness of fit. Highest PPARγ inhibitory activity was predicted for T3 and accordingly was synthesized. The successful synthesis of the compound was confirmed by TLC, IR, and NMR analysis. T3 inhibited PPARγ ($IC_{50} = 7.459$ μM) which was also supported by the molecular docking study. The docking study also revealed that T3 binds efficiently within the allosteric pocket of the PPARγ rather than the binding pocket and possess stronger interactions than the irreversible antagonist GW9662. Finally, T3 significantly inhibited adipocyte differentiation and lipid accumulation the differentiated adipocytes by downregulating the protein level expression of PPARγ ($IC_{50} = 7.8$ μM). The in silico prediction for PPARγ inhibitory activity of T3 was well corroborated by the in vitro experimental results. From the enzyme inhibition assay, it was noticeable that GW9662 (positive control) had better inhibition. But interestingly at the cellular level T3 exhibited higher antiadipogenic characteristics by downregulating PPARγ protein level expressions than GW9662. Further investigations of effect of T3 on protein and gene level expressions of other adipogenic factors can strongly establish the antiadipogenic potency of T3. To conclude our study, we strongly suggest T3 as a potential PPARγ inhibitor that significantly downregulates adipogenesis and differentiation, thereby conferring antiobesity potency to the newly synthesized conjugate.

Abbreviations

ANOVA	Analysis of variance
AP-1	Activation protein 1
BCS	Bovine calf serum
BSA	Bovine serum albumin
CNS	Central nervous system
CF	Caffeic acid
DCC	*N,N'*-Dicyclohexyl carbodimide
DMAP	4-Dimethylaminopyridine
DMEM	Dulbecco's modified eagle's medium
DMSO	Dimethyl sulfoxide
DMF	Dimethylformamide
FDA	Food and drug administration
GLP-1	Glucagon-like peptide 1
GABA	ɣ-Aminobutyric acid
GA	Genetic algorithm
HRP	Horseradish peroxidase
IBMX	3-Isobutyl-1-methyl xanthine
LBD	Ligand binding domain
LMO	Leave many out
LOF	Friedman lack of fit
LOO	Leave one out
MTT	(3-(4,5-Dimethylthiazol-2-yl)-2,5-diphenyltetrazolium bromide)
MLR	Multiple linear regression

MD	Molecular dynamics
NCCS	National Centre for Cell Science
NFκB	Nuclear factor kappa B
OECD	Organization for Economic Cooperation and Development
PCA	Principle component analysis
PPARγ	Peroxisome proliferator-activated receptor
PBS-T	Phosphate-buffered saline-Tween 20
QSAR	Quantitative structure–activity relationship
RMSD	Root mean square deviation
RMSF	Root mean square fluctuation
Rg	Radius of gyration
SMILES	Simplified molecular input line system
SDS-PAGE	Sodium dodecyl sulfate–polyacrylamide gel electrophoresis
SASA	Solvent accessible surface area
TR-FRET	Time-resolved fluorescence resonance energy transfer
TPM	Topiramate
TPAC	Topiramate–phenolic acid conjugates
T3	Topiramate–caffeic acid conjugate

Supplementary Information

The online version contains supplementary material available at https://doi.org/10.1186/s43094-024-00617-1.

Additional file 1. Supplementary data.

Acknowledgements
The authors sincerely acknowledge the School of Pharmaceutical Sciences, Siksha 'O' Anusandhan (Deemed to be University), Bhubaneswar, for carrying out the study.

Author contributions
IP performed investigation and original draft preparation. BB performed investigation. PGRA performed data curation, software handling, and draft reviewing. PPG performed software handling and writing. TS contributed to conceptualization, methodology, and draft reviewing and editing.

Funding
No funding was received for conducting the study.

Availability of data and material
All data generated or analyzed during this study are included in supplementary information files.

Declarations

Ethics approval and consent to participate
Not applicable.

Consent for publication
Not applicable.

Competing interest
The authors have no competing interests to declare that are relevant to the content of this article.

Author details
[1]Department of Pharmaceutical Chemistry, School of Pharmaceutical Sciences, Siksha 'O'Anusandhan (Deemed to be University), Bhubaneswar, Odisha 751003, India. [2]Department of Chemistry, ITER, Siksha 'O'Anusandhan (Deemed to be University), Bhubaneswar, Odisha 751030, India. [3]School of Biotechnology and Bioinformatics, D Y Patil Deemed to be University, Navi Mumbai, Maharashtra 400614, India.

Received: 9 December 2023 Accepted: 10 March 2024
Published online: 18 March 2024

References

1. Malik VS, Willet WC, Hu FB (2020) Nearly a decade on — trends, risk factors and policy implications in global obesity. Nat Rev Endocrinol 16:615–616. https://doi.org/10.1038/s41574-020-00411-y
2. Hanson P, Weickert MO, Barber TM (2020) Obesity: novel and unusual predisposing factors. Ther Adv Endocrinol Metab. https://doi.org/10.1177/2042018820922018
3. Barber TM, Dimitriadis GK, Andreou A, Franks S (2016) Polycystic ovary syndrome: insight into pathogenesis and a common association with insulin resistance. Clin Med 16:262–266. https://doi.org/10.7861/clinmedicine.16-3-262
4. Wang F, Han L, Hu D (2017) Fasting insulin, insulin resistance and risk of hypertension in the general population: a meta-analysis. Clin Chim Acta 464:57–63. https://doi.org/10.1016/j.cca.2016.11.009
5. Lam DCL, Lam KSL, Ip MSM (2014) Obstructive sleep apnoea, insulin resistance and adipocytokines. Clin Endocrinol 82:165–177. https://doi.org/10.1111/cen.12597
6. Avgerinos KI, Spyrou N, Mantzoros CS, Dalamaga M (2019) Obesity and cancer risk: emerging biological mechanisms and perspectives. Metabolism 92:121–135. https://doi.org/10.1016/j.metabol.2018.11.001
7. Klop B, Elte J, Cabezas M (2013) Dyslipidemia in obesity: mechanisms and potential targets. Nutrients 5:1218–1240. https://doi.org/10.3390/nu5041218
8. Bhat SP, Sharma A (2017) Current drug targets in obesity pharmacotherapy – a review. Curr Drug Targets 18:983–993. https://doi.org/10.2174/1389450118666170227153940
9. Francisco Bonamichi BD, Bezerra Parente E, dos Santos RB, Beltzhoover R, Lee J, Nunes Salles JE (2018) The challenge of obesity treatment: a review of approved drugs and new therapeutic targets. J Obes Eat Disord 4:1–10. https://doi.org/10.21767/2471-8203.100034
10. Jones BJ, Bloom SR (2015) The new era of drug therapy for obesity: the evidence and the expectations. Drugs 75:935–945. https://doi.org/10.1007/s40265-015-0410-1
11. Halpern B, Halpern A (2015) Safety assessment of FDA-approved (orlistat and lorcaserin) anti-obesity medications. Expert Opin Drug Saf 14:305–315. https://doi.org/10.1517/14740338.2015.994502
12. Velazquez A, Apovian CM (2018) Updates on obesity pharmacotherapy. Ann N Y Acad Sci 1411:106–119. https://doi.org/10.1111/nyas.13542
13. Picard F, Deshaies Y, Lalonde J, Samson P, Richard D (2000) Topiramate reduces energy and fat gains in lean (Fa/?) and obese (fa/fa) Zucker rats. Obes Res 8:656–663. https://doi.org/10.1038/oby.2000.84
14. Richard D, Picard F, Lemieux C, Lalonde J, Samson P, Deshaies Y (2002) The effects of topiramate and sex hormones on energy balance of male and female rats. Int J Obes Relat Metab Disord 26:344–353. https://doi.org/10.1038/sj.ijo.0801873
15. Martins GP, Souza CO, Marques SD, Luciano TF, da Silva Pieri BL, Rosa JC, Da Silva AS, Pauli JR, Cintra DE, Ropelle ER, Rodrigues B (2015) Topiramate effects lipolysis in 3T3-L1 adipocytes. Biomed Rep 3:827–830. https://doi.org/10.3892/br.2015.514
16. Ozdal T, Sela DA, Xiao J, Boyacioglu D, Chen F, Capanoglu E (2016) The reciprocal interactions between polyphenols and gut microbiota and effects on bioaccessibility. Nutrients 8:78. https://doi.org/10.3390/nu8020078
17. Rodríguez-Pérez C, Segura-Carretero A, del Mar CM (2019) Phenolic compounds as natural and multifunctional anti-obesity agents: a review. Crit Rev Food Sci Nutr 59:1212–1229. https://doi.org/10.1080/10408398.2017.1399859
18. Willson TM, Lambert MH, Kliewer SA (2001) Peroxisome proliferator–activated receptor γ and metabolic disease. Annu Rev Biochem 70:341–367. https://doi.org/10.1146/annurev.biochem.70.1.341
19. Gray S, Dalla Nora E, Vidal-Puig A (2005) Mouse models of PPAR-γ deficiency: dissecting PPAR-γ's role in metabolic homoeostasis. Biochem Soc Trans 33:1053–1058. https://doi.org/10.1042/BST0331053
20. Tontonoz P, Spiegelman BM (2008) Fat and beyond: the diverse biology of PPARγ. Annu Rev Biochem 77:289–312. https://doi.org/10.1146/annurev.biochem.77.061307.091829
21. Frkic RL, Marshall AC, Blayo AL, Pukala TL, Kamenecka TM, Griffin PR, Bruning JB (2018) PPARγ in complex with an antagonist and inverse agonist: a tumble and trap mechanism of the activation helix. I Sci 5:69–79. https://doi.org/10.1016/j.isci.2018.06.012

22. Ricote M, Glass CK (2007) PPARs and molecular mechanisms of transrepression. Biochim Biophys Acta Mol Cell Biol Lipids 1771:926–935. https://doi.org/10.1016/j.bbalip.2007.02.013
23. Sun H, Kim JK, Mortensen R, Mutyaba LP, Hankenson KD, Krebsbach PH (2013) Osteoblast-targeted suppression of PPARγ increases osteogenesis through activation of mTOR signaling. Stem cells 31:2183–2192. https://doi.org/10.1002/stem.1455
24. Duque G, Li W, Vidal C, Bermeo S, Rivas D, Henderson J (2013) Pharmacological inhibition of PPARγ increases osteoblastogenesis and bone mass in male C57BL/6 mice. J Bone Miner Res 28:639–648. https://doi.org/10.1002/jbmr.1782
25. Wang X, Sun Y, Wong J, Conklin D (2013) PPARγ maintains ERBB2-positive breast cancer stem cells. Oncogene 32:5512–5521. https://doi.org/10.1038/onc.2013.217
26. Dash R, Biswal J, Yadav M, Sharma T, Mohapatra S, Prusty SK (2023) Novel atorvastatin-curcumin conjugate nanogel, a selective COX2 inhibitor with enhanced biopharmaceutical profile: design, synthesis, in silico, in vitro, and in vivo investigation. J Drug Deliv Sci Technol 81:104211. https://doi.org/10.1016/j.jddst.2023.104211
27. Rath B, Qais FA, Patro R, Mohapatra S, Sharma T (2021) Design, synthesis and molecular modeling studies of novel mesalamine linked coumarin for treatment of inflammatory bowel disease. Bioorg Med Chem Lett 41:128029. https://doi.org/10.1016/j.bmcl.2021.128029
28. Hu M, Huang P, Wang Y, Su Y, Zhou L, Zhu X, Yan D (2015) Synergistic combination chemotherapy of camptothecin and floxuridine through self-assembly of amphiphilic drug–drug conjugate. Bioconjug Chem 26:2497–2506
29. Gilson MK, Liu T, Baitaluk M, Nicola G, Hwang L, Chong J (2016) BindingDB in 2015: a 141 public database for medicinal chemistry, computational chemistry and systems pharmacology. Nucleic Acids Res 44:D1045–D1053. https://doi.org/10.1093/nar/gkv1072
30. Yap CW (2011) PaDEL-descriptor: an open source software to calculate molecular descriptors and fingerprints. J Comput Chem 32:1466–1474
31. Toropova AP, Toropov AA (2018) CORAL: QSAR models for carcinogenicity of organic compounds for male and female rats. Comput Biol Chem 72:26–32. https://doi.org/10.1016/j.compbiolchem.2017.12.012
32. Toropov AA, Achary PG, Toropova AP (2016) Quasi-SMILES and nano-QFPR: the predictive model for zeta potentials of metal oxide nanoparticles. Chem Phys Lett 660:107–110. https://doi.org/10.1016/j.cplett.2016.08.018
33. Achary PGR, Toropova AP, Toropov AA (2019) Combinations of graph invariants and attributes of simplified molecular input-line entry system (SMILES) to build up models for sweetness. Food Res Int 122:40–46. https://doi.org/10.1016/j.foodres.2019.03.067
34. Toropov AA, Toropova AP (2017) The index of ideality of correlation: A criterion of predictive potential of QSPR/QSAR models? Mutat Res Toxicol Environ Mutagen 819:31–37. https://doi.org/10.1016/j.mrgentox.2017.05.008
35. Achary PGR (2014) Simplified molecular input line entry system-based optimal descriptors: QSAR modelling for voltage-gated potassium channel subunit Kv7.2. SAR QSAR Environ Res 25:73–90. https://doi.org/10.1080/1062936x.2013.842930
36. Gramatica P, Chirico N, Papa E, Cassani S, Kovarich S (2013) QSARINS: a new soft- ware for the development, analysis, and validation of QSAR MLR models. J Comput Chem 34:2121–2132. https://doi.org/10.1002/jcc.23361
37. Pettersen EF, Goddard TD, Huang CC et al (2004) UCSF Chimera–a visualization system for exploratory research and analysis. J Comput Chem 25:1605–1612. https://doi.org/10.1002/jcc.20084
38. Trott O, Olson AJ (2010) AutoDock Vina: improving the speed and accuracy of docking with a new scoring function, efficient optimization, and multithreading. J Comput Chem 31:455–461
39. Berendsen HJ, van der Spoel D, van Drunen R (1995) GROMACS: a message-passing parallel molecular dynamics implementation. Comput Phys Commun 91:43–56. https://doi.org/10.1016/0010-4655(95)00042-e
40. Hess B, Bekker H, Berendsen HJ, Fraaije JG (1997) LINCS: a linear constraint solver for molecular simulations. J Comput Chem 18:1463–1472. https://doi.org/10.1002/(sici)1096-987x(199709)18:12%3c1463::aid-jcc4%3e3.0.co;2-h
41. Andrade CK, Rocha RO, Vercillo OE, Silva WA, Matos RA (2003) DCC/DMAP-mediated coupling of carboxylic acids with oxazolidinones and thiazolidinethiones. Synlett 2003:2351–2352. https://doi.org/10.1055/s-2003-42117
42. Savjani JK, Mulamkattil S, Variya B, Patel S (2017) Molecular docking, synthesis and biological screening of mefenamic acid derivatives as anti-inflammatory agents. Eur J Pharmacol 801:28–34. https://doi.org/10.1016/j.ejphar.2017.02.051
43. van Zadelhoff A, Vincken JP, de Bruijn WJC (2022) Facile amidation of non-protected hydroxycinnamic acids for the synthesis of natural phenol amides. Molecules 27:2203. https://doi.org/10.3390/molecules27072203
44. Peng Y, Zhang Q, Zielinski RM, Howells RD, Welsh WJ (2020) Identification of an irreversible PPARγ antagonist with potent anticancer activity. Pharmacol Res Perspect 8:e00693. https://doi.org/10.1002/prp2.693
45. Lee SG, Lee YJ, Jang MH, Kwon TR, Nam JO (2017) Panax ginseng leaf extracts exert anti-obesity effects in high-fat diet-induced obese rats. Nutrients 9:999. https://doi.org/10.3390/nu9090999
46. Friedman H (1991) Multivariate adaptive regression splines. Ann Stat 19:1–67. https://doi.org/10.1214/aos/1176347963
47. Consonni V, Ballabio D, Todeschini R (2009) Comments on the definition of the Q2 parameter for QSAR validation. J Chem Inf Model 49:1669–1678. https://doi.org/10.1021/ci900115y
48. Dewar MJ, Zoebisch EG, Healy EF, Stewart JJ (1985) Development and use of quantum mechanical molecular models. 76. AM1: a new general purpose quantum mechanical molecular model. J Am Chem Soc 107:3902–3909. https://doi.org/10.1021/ja00299a024
49. Todeschini R, Consonni V (2000) Handbook of molecular descriptors. Wiley, New Jersey. https://doi.org/10.1002/9783527613106
50. Rezić T, Presečki AV, Kurtanjek Ž (2021) New approach to the evaluation of lignocellulose derived by-products impact on lytic-polysaccharide monooxygenase activity by using molecular descriptor structural causality model. Bioresour Technol 342:125990. https://doi.org/10.1016/j.biortech.2021.125990
51. Krishnasamy C, Raghuraman A, Kier LB, Desai UR (2008) Application of molecular connectivity and electro-topological indices in quantitative structure-activity analysis of pyrazole derivatives as inhibitors of factor Xa and Thrombin. Chem Biodivers 5:2609–2620. https://doi.org/10.1002/cbdv.200890216
52. Miyachi H (2023) Structural biology inspired development of a series of human peroxisome proliferator-activated receptor gamma (PPARγ) ligands: from agonist to antagonist. Int J Mol Sci 24:3940. https://doi.org/10.3390/ijms24043940
53. Almahmoud S, Elix CC, Jones JO, Hopkins CR, Vennerstrom JL, Zhong HA (2021) Virtual screening and biological evaluation of PPARγ antagonists as potential anti-prostate cancer agents. Bioorg Med Chem 46:116368. https://doi.org/10.1016/j.bmc.2021.116368
54. Asteian A, Blayo AL, He Y, Koenig M, Shin Y, Kuruvilla DS, Corzo CA, Cameron MD, Lin L, Ruiz C, Khan S (2015) Design, synthesis, and biological evaluation of indole biphenylcarboxylic acids as PPARγ antagonists. ACS Med Chem Lett 6:998–1003. https://doi.org/10.1021/acsmedchemlett.5b00218
55. Sivamani Y, Shanmugarajan D, Kumar TD, Faizan S, Channappa B, Naishima NL, Kumar BP (2021) A promising in silico protocol to develop novel PPARγ antagonists as potential anticancer agents: design, synthesis and experimental validation via PPARγ protein activity and competitive binding assay. Comput Biol Chem 95:107600. https://doi.org/10.1016/j.compbiolchem.2021.107600
56. Montanari R, Capelli D, Yamamoto K, Awaishima H, Nishikata K, Barendregt A, Heck AJ, Loiodice F, Altieri F, Paiardini A, Grottesi A (2020) Insights into PPARγ phosphorylation and its inhibition mechanism. J Med Chem 63:4811–4823. https://doi.org/10.1021/acs.jmedchem.0c00048
57. Hasan MU (1980) ^{13}C NMR spectra of some amides and imides. Effect of inductive and mesomeric interactions, cyclization and hydrogen bonding on ^{13}C NMR chemical shifts. Org Magn Reson 14:447–450. https://doi.org/10.1002/mrc.1270140605
58. Li D, Zhang F, Zhang X, Xue C, Namwanje M, Fan L, Reilly MP, Hu F, Qiang L (2016) Distinct functions of PPARγ isoforms in regulating adipocyte plasticity. Biochem Biophys Res Commun 481:132–138. https://doi.org/10.1016/j.bbrc.2016.10.152

Publisher's Note